Report no. changed (Mar 2006): SM-359-UU

SACLANTCEN MEMORANDUM
serial no.: SM-359

SACLANT UNDERSEA
RESEARCH CENTRE
MEMORANDUM

BROAD-BAND GEO-ACOUSTIC INVERSION IN SHALLOW WATER FROM WAVEGUIDE RESPONSE MEASUREMENTS ON A SINGLE HYDROPHONE: THEORY AND YELLOW SHARK EXPERIMENTAL RESULTS

J.-P. Hermand

May 1999

Report no. changed (Mar 2006): SM-359-UU

SACLANT Undersea Research Centre
Viale San Bartolomeo 400
19138 San Bartolomeo (SP), Italy

tel: +39-0187-5271
fax: +39-0187-524.600

e-mail: library@saclantc.nato.int

NORTH ATLANTIC TREATY ORGANIZATION

Broad-Band Geoacoustic Inversion in Shallow Water from Waveguide Impulse Response Measurements on a Single Hydrophone: Theory and Experimental Results

Jean-Pierre Hermand

The content of this document pertains to work performed under Project 013-1 of the SACLANTCEN Programme of Work. The document has been approved for release by The Director, SACLANTCEN.

Jan L. Spoelstra
Director

intentionally blank page

Broad-Band Geoacoustic Inversion in Shallow Water from Waveguide Impulse Response Measurements on a Single Hydrophone: Theory and Experimental Results

Jean-Pierre Hermand

Executive Summary: Performance models such as the Allied Environmental Support System (AESS) require environmental input parameters such as the geoacoustic properties of the battlespace. The models ingest the input parameters from databases to predict the ASW and MCM performance in the operating area. These databases have a scarcity of data, particularly in littoral environments. A Rapid Environmental Assessment (REA) technique has been devleoped which allows for the determination of the geoacoustic properties without resorting to large acoustic receiving apertures. The method is based on reception of broadband acoustic signals and modelling the littoral environment between the acoustic transmitter and a signal receiving hydrophone. In addition, the technique has been extended to drifting sonobuoys such that the bottom properties of the battlespace can be determined remotely. This report presents the measurement and modelling results and demonstrates that the bottom features can be resolved.

Report no. changed (Mar 2006): SM-359-UU

intentionally blank page

Contents

1

Introduction

Modern geoacoustic inversion techniques for shallow water environments seek to exploit the spatial and temporal structure of waterborne pressure wavefields.

In this paper, the time dispersion and attenuation characteristics of the acoustic waveguide are explicitly used to resolve bottom properties from single-hydrophone measurements of propagating broad-band waveforms.

Numerous variations of the "matched field" concept [1, 2] have been investigated to localize an unknown sound source [3, 4, 5, 6] and later on, to characterize an unknown environment [7, 8, 9, 10]. Linear perturbative methods [11, 12] were developed as an alternative to nonlinear inverse methods. All these methods match the spatial structure of the complex pressure field, in the horizontal or vertical planes, at one or more discrete frequencies. The literature dealing with the spatiotemporal structure of the wavefield for the purpose of environmental inversion is limited as indicated by the review of the state of the art [13] and recent publications [14, 15].

Related experimental studies relied on acoustic measurements configurations involving either bottom-moored vertical arrays (VA) [16, 17, 18, 19], synthetic horizontal apertures [20, 21] or sound sources and horizontal line arrays towed simultaneously [10]. These require considerable ship time in surveying large areas of the shallow continental shelf where upper sediments typically exhibit marked variability.

The *Yellow Shark* experiments performed in the Giglio basin, off the west coast of Italy, during the fall of 1994 (YS94) and the spring of 1995 (YS95) were primarily designed to develop and validate inversion techniques based on sparse, waterborne measurements of the acoustic-channel transfer function [22]. The CW transmissions of conventional MFP experiments were replaced by broad-band-coded (200–1600 Hz) waveforms generated from bottom-moored calibrated acoustic projectors. The signals, propagated over distances of 8–55 km, were received on sparse (4 elements) and dense (64/32 elements) VA's. The *EnVerse* sea trials conducted in part south of Marettimo island, off Sicily, during the winter of 1997 (EV97), extended the perfectly static configurations of *Yellow Shark* to an advanced drifting acoustic buoy field for the rapid assessment of range-dependent (RD) bottom properties over a 12 × 8 km wide area [23, 24].

In a recent study [13], bottom geoacoustic parameters were inverted from broad-band matched-field processing (BMFP) of multitone pressure fields sampled on a 63 m 32-element VA in a 15 km mildly range-dependent (RD), soft-bottom, shallow-water medium, northwest of Formiche di Grosseto islands [YS94, transect XF, Fig. 1]. The wide (200–800 Hz) range of tones was necessary and sufficient to resolve correctly the bottom.

In an earlier paper [25], the feasibility of inferring bottom properties from transfer function measurements between a source and a single-depth receiver was investigated numerically for the Giglio basin platform. Modeled Green's functions were shown to be highly sensitive to small variations of archival geophysical/geoacoustic bottom parameters, irrespective of source/receiver geometry.

In the present study, a single-hydrophone, geoacoustic inversion technique is proposed and demonstrated experimentally with YS94 data. The broad bandwidth of the probing signal is utilized to determine bottom properties. An environmentally-adaptive processor, the model-based matched filter (MBMF), fully integrates the physics of wave propagation into its reference signals (replicas) [26]. The concept was applied successfully for source localization in fading time-dispersive ocean channels [27]. In essence, the MBMF is a close relative of the "matched signal" (MESS) processor which was demonstrated experimentally by backpropagating a received signal and effectively refocusing the energy at the source [28, 29]. Here, for the purpose of environmental inversion from one-way transmission measurements, the process is performed numerically at the receiver by means of broad-band modeling and time-domain correlation. The frequency-dependent attenuation, multipath and time dispersion effects due in part to bottom interaction are incorporated into the MBMF replicas as a function of candidate models. Environmental matching occurs when most of the time-spread energy is recombined *coherently* by the MBMF receiver.

In related papers [30, 31], RD bottom properties were determined from broad-band transmission loss (TL) measurements, sparse in range and depth, in a strongly RD situation [YS95, transect EF in Fig. 1]. In this frequency-averaged incoherent processing, the data-model matching requirements are less stringent than for space-time coherent processing. Considerable robustness of bottom estimates to environmental variability was obtained to the detriment of resolution.

The present work features 1) geoacoustic inversion based on the acoustic-channel impulse response measured on a single hydrophone over a wide *continuum* of frequencies (200–800 Hz), 2) transmission of large time-bandwidth (TB) product waveforms and matched filter processing for optimum reception and inversion, 3) objective function derived from the MBMF gain relative to the conventional matched filter, 4) Green's function synthesis with RI and RD coupled normal mode propagation models, 5) exhaustive search over bottom parameter spaces with up to 8 dimensions to determine actual ambiguity and resolution properties, 6) statistical analysis of the solutions, 7) constrained nonlinear parametric optimization for fast execution time in place of combinatorial search, 8) comparison of single-element inversion results with those obtained from space-coherent MBMF processing over a 63 m 32-element VA, 9) comparison with results obtained under identical conditions from BMFP inversion of multitone continuous-wave (CW) pressure fields over the same frequency band, 10) measurements over different propagation distances, 11) accurately known geometries, not inverted, 12) detailed hydrographical measurements supporting the inversion, 13) validation with independent geophysical characterization of the sea bottom including specialized sediment core data.

The YS94 experiments were reported in [22, 13]. Additional sediment cores acquired after YS95 are analyzed in Annex A. In Section 2, the measurements of the acoustic-channel impulse response are described. A RD environmental model constructed from *in situ* hydrographical and geophysical measurements is described. In Section 3, metrics and objective functions for MBMF inversion are derived from previous theoretical results. In Section 4, the approach to modeling, signal processing and inversion of the acoustic data is outlined. In Section 5, results from single-depth, depth-average and space-coherent MBMF inversion runs are discussed. The emphasis is on observability and resolvability of the bottom from single-depth measurements, uniqueness and robustness of the bottom inverses. The experimental results are validated with a "ground truth" bottom model and compared with earlier BMFP inversion results. Section VI concludes the paper.

2

Broad-Band Inversion Experiments

During the *Yellow Shark* sea trials in the summer of 1994 and the spring of 1995 over 10^5 acoustic signals in the frequency band 200–1600 Hz were propagated between fixed sound sources and receiving vertical arrays (VA) along four transects in the Giglio basin and platform, off the west coast of Italy. The acoustic-channel impulse response measurements analyzed in this paper were obtained in September 1994 over a mildly range-dependent (RD) transect in the basin platform, northwest of the islands of Formiche di Grosseto. Procedures for acoustic and environmental measurements were described in [13]. In this section, information specific to the investigated acoustic data set is provided. The geoacoustic model of the Giglio basin platform [13] is refined on the basis of complementary sediment cores collected in 1996.

2.1 Experimental Configuration

A map of the experimental area in Fig. 1 shows the location of the acoustic and oceanographic moorings and of the corings. Fig. 2 shows the configuration of the acoustic moorings.

2.2 Impulse Response Measurements

Large time-bandwidth-product signals: The signal $s(t)$ transmitted to measure the band-limited impulse response of the acoustic channel consisted of a long (duration $\Delta t = 12$ s), broad-band (center frequency $f_0 = 500$ Hz, bandwidth $\Delta f = 600$ Hz), linearly frequency modulated (LFM) waveform. In spite of self clutter in the time domain, LFM coding was preferred to a binary M-sequence [33] to exploit fully the limited frequency band of the flextensional projector by minimizing instantaneous bandwidth [34].

Source equalization: The LFM waveform was modulated in amplitude to equalize the transmitting sensitivity response (TSR) of the projector. The complex envelope of $s(t)$ is approximately given by

$$\tilde{s}(t) = \mathrm{equ}(t/\Delta t)\exp(j2\pi\Delta f t^2/2\Delta t). \tag{1}$$

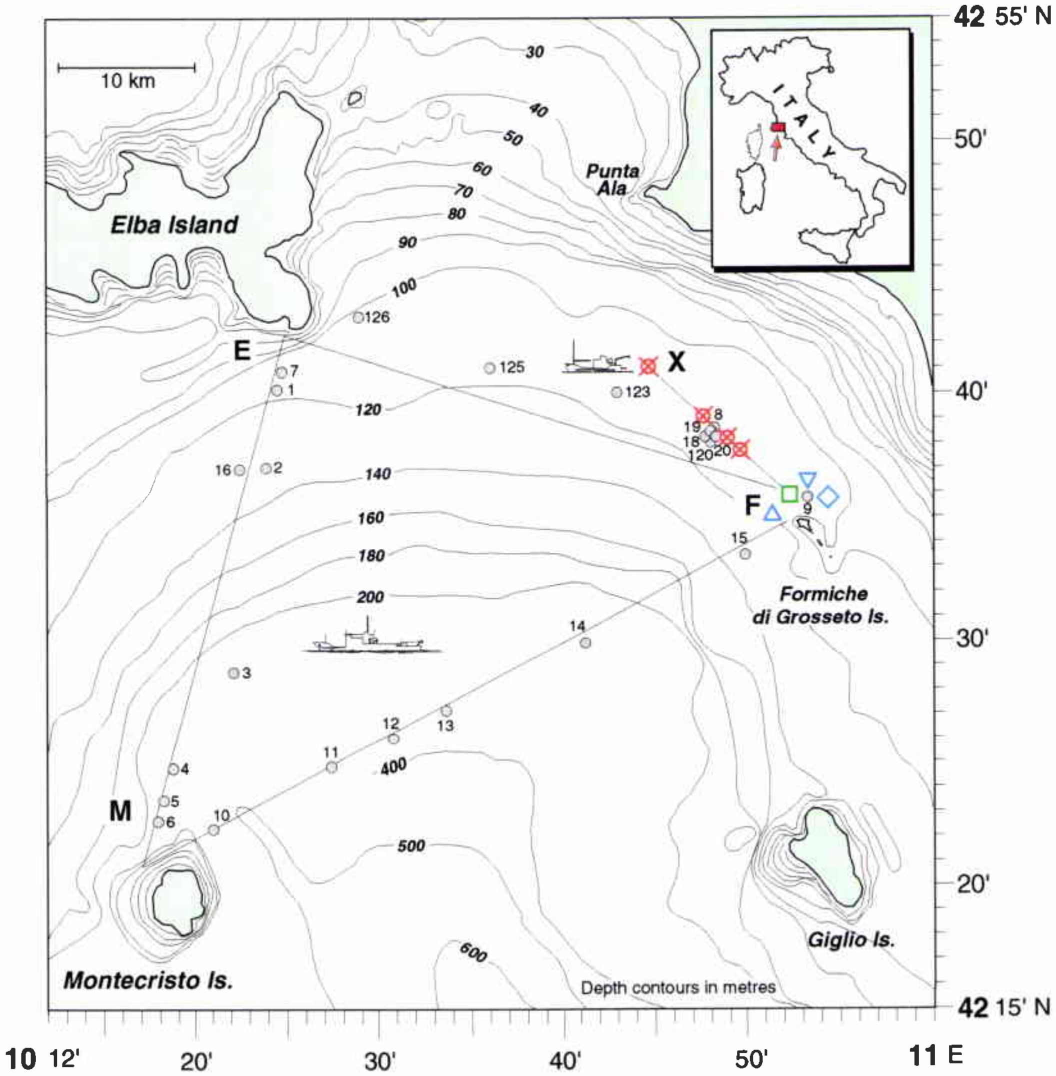

Figure 1 *Map of the* Yellow Shark 94 *experimental configuration. The moorings, northwest of Formiche di Grosseto islands, are identified with the following symbols. ⊗: sound source, □: vertical array, ◇: waverider buoy, △: currentmeter chain, and ▽: meteo buoy. Coring locations are numbered and marked by a ● symbol. See [32] for cores 120, 123, 125 and 126 and [22] for cores 1–16. Cores 18–20 are documented in this paper.*

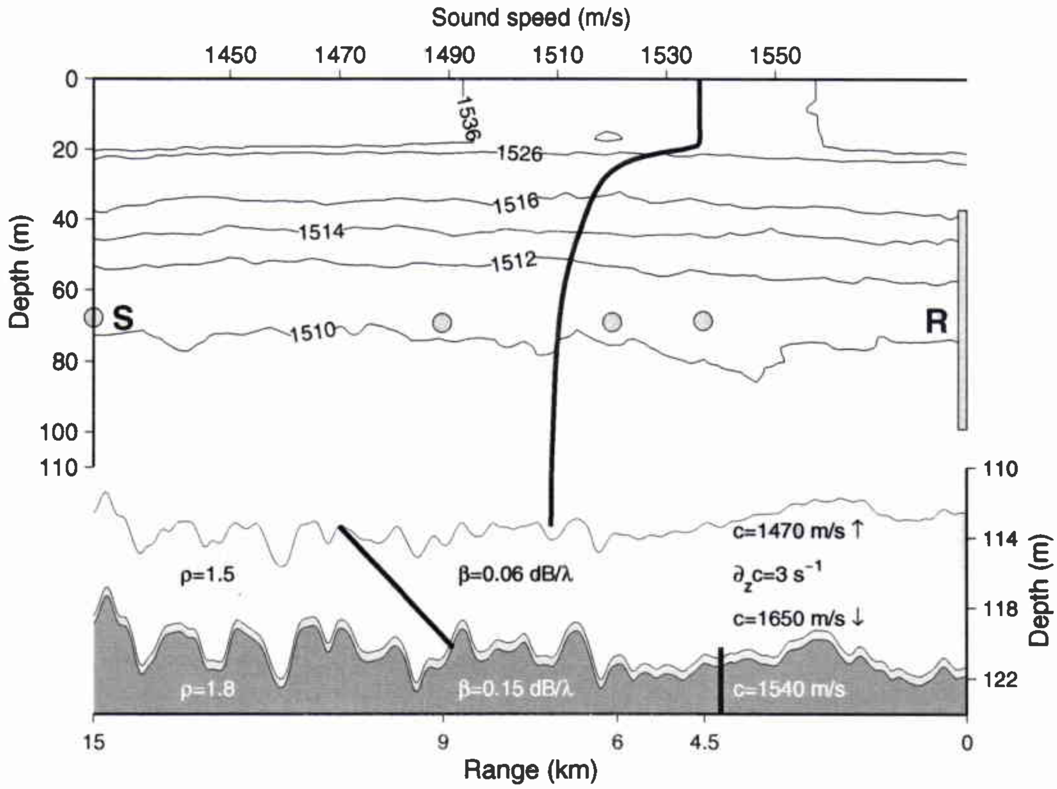

Figure 2 *Experimental geometry and range-dependent environmental model for the* Yellow Shark *15 km transect XF northwest of Formiche di Grosseto islands, off the west coast of Italy. Source (circles) and vertical array (bar) positions are indicated. The upper scale refers to the range-averaged ocean and bottom sound speed profiles (solid lines). The clay layer and silty clay bottom with the grainstone interface are represented in gray. The model is based on ocean sound speed profiles and bottom geoacoustic properties measured* in situ.

Table 1 *Acoustic and CTD data recordings along transect XF*

Day	Range	Acoustic data		CTD data		Sel.
	(m)	Period	#	Period	#	time
10 Sept 94	15021	1012–1242	71	0930–1221	62	1050
	9026	1740–1948	49	1724–1855	34	1808
11 Sept 94	6087	0732–0820	25	0600–0706	25	0732
	4524	1318–1418	31	1228–1317	25	1318

Time refers to UTC. The transmission times of the pings selected for inversion are indicated in the last column. See [13] for corresponding multitone signal transmissions. See [22] for details regarding the acoustical and oceanographical runs.

The equalization function equ is defined by

$$\mathrm{equ}(x) = \begin{cases} |F(\omega_0 + x\Delta\omega)|^{-1}, & \text{for } |x| \leq \frac{1}{2}; \\ 0, & \text{elsewhere.} \end{cases} \qquad (2)$$

where $|F(\omega)|$ is a measured TSR normalized to unit gain. The transmitted signals (pings) were measured in water by a pole-mounted hydrophone in the far field of the projector.

2.3 Acoustic Data

A total of 176 pings were transmitted (Table 1).

Measurement reproducibility: Figure 3 shows the matched-filtered signals received on four VA elements over the period of each run. The overall ping-to-ping variability was low and the temporal trends of the dispersed arrivals were correlated to the slowly time-varying thermocline thickness. Short-term variability was stronger in the VA upper part where sound speed gradients were large and sensitive to near-surface effects. The signal-to-noise ratio (SNR) and signal time coherence were sufficiently high for inversion at all ranges and depths.

Energy time spreading: Fig. 4 shows the total energy and time spreading *versus* depth at each range, at the MF output. The energy was normalized to its maximum at 4.5 km range. The energy time spreading was characterized by

$$\sigma_t^2 = \langle t^2 \rangle - \langle t \rangle^2 \qquad (3)$$

where the mean time $\langle t \rangle$ is defined as

$$\langle t \rangle = \int t|y(t)|^2 dt \qquad (4)$$

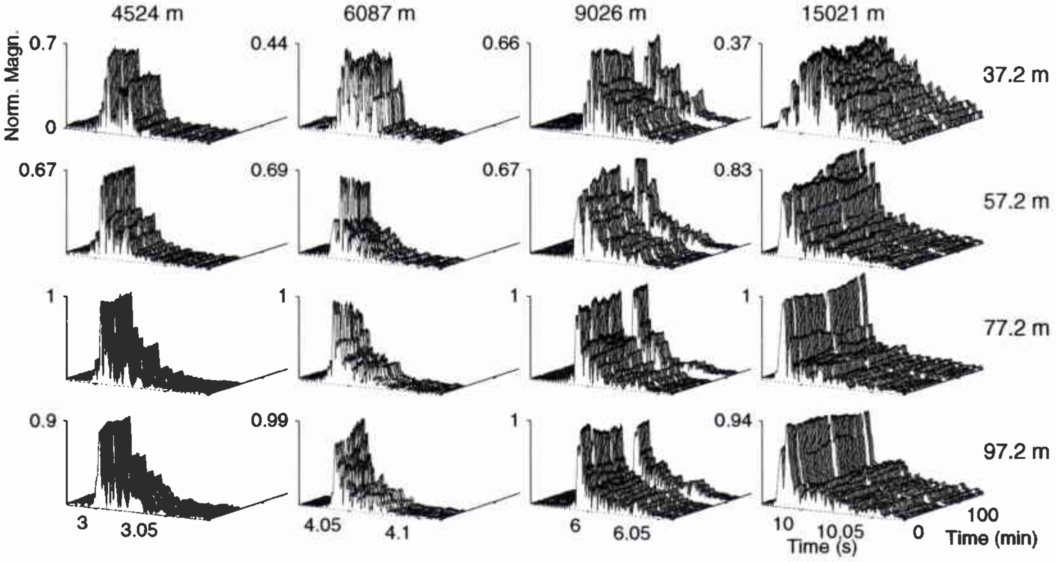

Figure 3 *Matched-filter envelope outputs at 37.2 m, 57.2 m, 77.2 m and 97.2 m water depths (from top to bottom) and 4.5 km, 6 km, 9 km and 15 km ranges (from left to right). The envelopes were normalized for each range separately. Travel times were determined accurately from differential GPS ranges and GPS-clock-synchronized transmission and reception times. Elapsed times refer to the first transmission of each run. Some pings were missing.*

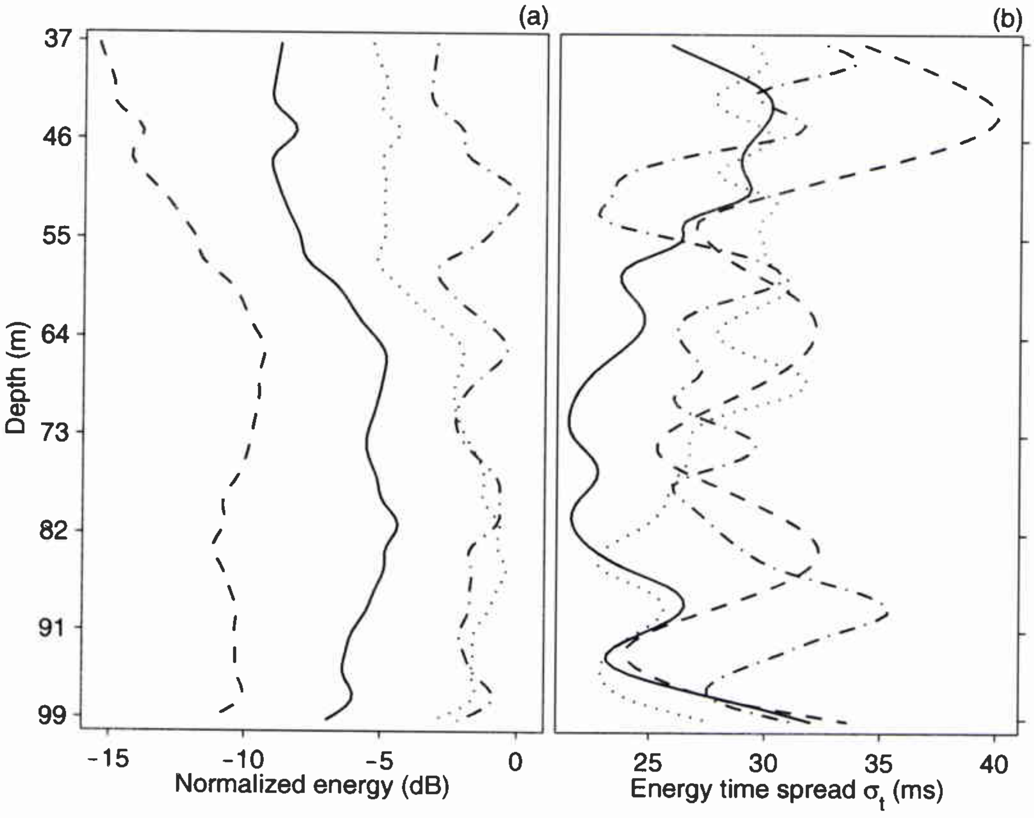

Figure 4 *Waveguide impulse response characteristics* versus *depth: (a) normalized total energy and (b) time spreading for the ranges of 4.5 km (dash-dot), 6 km (dot), 9 km (solid), and 15 km (dash). The signal realizations from each run (Table 1) were ensemble averaged.*

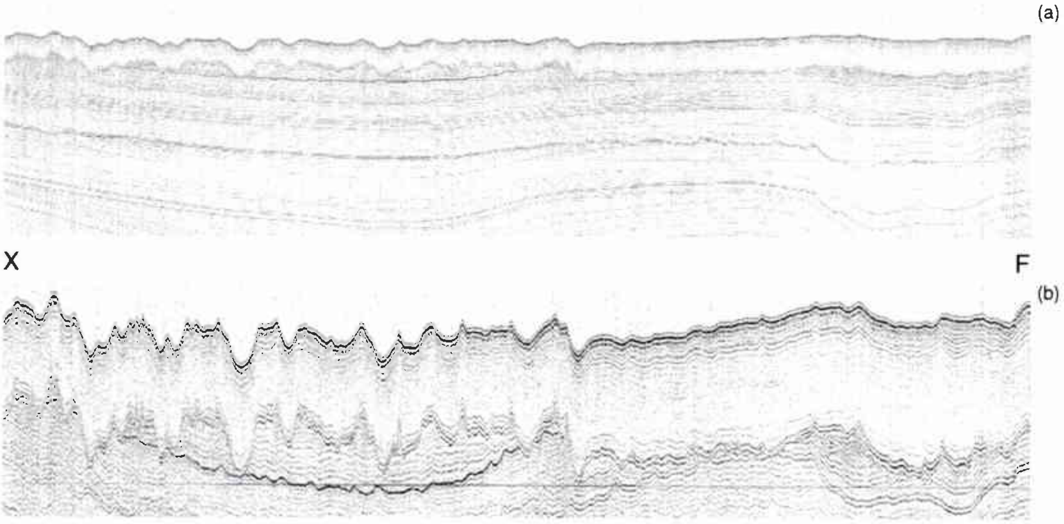

Figure 5 *Seismic reflection profile of the surficial sediment layers along transect XF, northwest of Formiche di Grosseto islands: (a) deep profile, (b) clay layer. Acoustic mooring locations, and range and depth scales are indicated in Fig. 1. The profile was obtained with short pulses of 1 ms duration and 300 J energy transmitted every 0.7 s from a boomer and received on a short 10 element array both towed right below the sea surface at a speed of 2.3 m/s. The depth-averaged water sound speed was 1508.1 m/s.*

and the mean duration $\langle t^2 \rangle$ is defined similarly. The energy time spreading is large ($2\sigma_t$ =22–40 ms) with respect to the time resolution of the probing signal ($1/\Delta f$ = 1.7 ms). The depth and range dependence relates to the modal composition, as shown later. The frequency band was sufficiently wide to observe, at all depths and ranges, the time dispersion characteristics of the acoustic channel which are central to the inversion technique discussed here.

2.4 Oceanographic and Geophysical Data

Environmental data were reported in [13]. Figs. 5 and 6 in [13] show the range-dependent ocean SSP measured along transect XF during the acoustic transmissions. The high-resolution, single-channel, seismic reflection profile in Fig. 5 shows the sediment layering along the 15 km transect XF. Analysis of sediment cores collected near the mid point of transect XF is given in Annex A.

2.5 Range-Dependent Environmental Model

Fig. 2 depicts a RD environmental model of the transect XF. This simplified model, considered as our ground truth, was derived from

- 2-D ocean CTD profiles (SSP),
- bathymetry,
- acoustic stratigraphy,
- mass properties and sound speed profiles of sediment cores [32, 35, 22],
- inversion of angle-dependent bottom reflection data [13],
- geological interpretation [36, 37, 38],
- early TL data/model comparison [39], and
- BMFP geoacoustic inversion [13].

The displayed 2-D sound speed structure was measured during the 15 km LF acoustic run [Fig. 5(c),(e) and (h) in [13] for the 9 km, 6 km and 4.5 km runs, respectively]. The acoustic propagation was determined by a strongly downward refracting, late summer temperature profile, below a well-developed thermocline. The mixed-layer thickness (20 m) was slowly time-varying with mild range dependence. The bottom is nearly flat (111–116 m) and characterized by a low-speed clay layer of variable thickness (5–9 m) overlying a higher-speed silty clay bottom with grainstone at the interface; the subbottom is made of similar consolidated sediments. Sound speed and gradient in the top sediment layer are mildly range dependent. Table 1 indicates the CTD data recording periods. See Table II in [13] for descriptive statistics of the mixed-layer thickness, water depth and top-sediment-layer thickness for the four measuring ranges.

3

Model-Based Matched Filter Inversion

In this section, signal processing and metrics for single-hydrophone inversion are derived. The signal processor is the model-based matched filter developed and applied for source localization in fading time-dispersive ocean channels [27].

3.1 Model-Based Receiver

We assume that the transmitted signal $s(t)$ propagates through a deterministic stationary ocean medium characterized by a Green's function $G(t, \mathbf{r})$, where $\mathbf{r}$ is the difference in radius vectors between the point source and receiver. The received signal $r(t, \mathbf{r})$ is the convolution of $s(t)$ and the time-invariant impulse response of the channel $g(t, \mathbf{r})$ and is perturbed by an additive, zero-mean, stationary Gaussian noise process $n(t)$. The receiver input $x(t, \mathbf{r})$ is given by

$$x(t, \mathbf{r}) = r(t, \mathbf{r}) + n(t) = g(t, \mathbf{r}) \otimes s(t) + n(t) \tag{5}$$

where $\otimes$ denotes convolution. Consider a receiver with time-invariant impulse response $h(t)$ and output $y(t, \mathbf{r})$,

$$y(t, \mathbf{r}) = h(t) \otimes x(t, \mathbf{r}). \tag{6}$$

The signal-to-mean noise power ratio (SNR) $\rho(t, \mathbf{r})$ of $y(t, \mathbf{r})$ is chosen as the criterion for optimization of $h(t, \mathbf{r})$. The upper bound on $\rho(t, \mathbf{r})$ is given by

$$\rho(t, \mathbf{r}) \leq \frac{2}{\pi N_0} \int_0^\infty |R(\omega, \mathbf{r})|^2 \mathrm{d}\omega \equiv \frac{2\mathcal{E}_r}{N_0} \equiv \rho_{\max}(\mathbf{r}), \ \forall t, \tag{7}$$

where $N_0/2$ is the power spectral density of $n(t)$ assumed to be white, $R(\omega, \mathbf{r})$ is the received energy spectrum,

$$R(\omega, \mathbf{r}) = G(\omega, \mathbf{r}) S(\omega) \tag{8}$$

where $S(\omega)$ is the transmitted energy spectrum and $G(\omega, \mathbf{r})$ is the transfer function of the channel (Fourier transform of the Green's function), and $\mathcal{E}_r$ is the received energy.

For large time-bandwidth-product signals $s(t)$ which satisfy the condition $\Delta t(\Delta\omega)^2/\omega_0 \gg 2\pi$, the expression for $\rho_{\max}$ reduces to

$$\rho_{\max}(\mathbf{r}) = \frac{2\mathcal{E}_s}{N_0}\beta(\mathbf{r}) \tag{9}$$

where

$$\beta(\mathbf{r}) \equiv \frac{1}{\Delta\omega}\int_\Omega |G'(\omega,\mathbf{r})|^2 \mathrm{d}\omega, \tag{10}$$

Ω is the frequency band of transmission, $\mathcal{E}_s = S_0\Delta\omega/2\pi$ is the transmitted energy and $\mathcal{E}_r = \mathcal{E}_s\beta(\mathbf{r})$ is the received energy. The prime symbol indicates here and henceforth that an arbitrary mean time delay is removed from the phase factor.

Let us define the model-based matched filter (MBMF) with frequency response

$$\mathcal{H}(\omega,\mathbf{r}) = \mathcal{H}_0\mathcal{G}'^*(\omega,\mathbf{r})S^*(\omega)\exp(-j\omega\tau) \tag{11}$$

where $\mathcal{H}_0$ is an arbitrary gain factor and $\mathcal{G}'$ denotes a predicted transfer function. The SNR at the MBMF receiver output is given by [27]

$$\rho(t,\mathbf{r}) = \rho_{\max}(\mathbf{r})|\mathcal{R}_{G'\mathcal{G}'}(\xi,\mathbf{r})|^2 \tag{12}$$

where ξ is a phase variable and $\mathcal{R}_{G'\mathcal{G}'}(\xi,\mathbf{r})$ is the complex-valued correlation

$$\mathcal{R}_{G'\mathcal{G}'}(\xi,\mathbf{r}) = \frac{\int_\Omega G'(\omega,\mathbf{r})\mathcal{G}'^*(\omega,\mathbf{r})\exp(j\omega\xi)\mathrm{d}\omega}{\left(\int_\Omega |G'(\omega,\mathbf{r})|^2\mathrm{d}\omega\int_\Omega |\mathcal{G}'(\omega,\mathbf{r})|^2\mathrm{d}\omega\right)^{1/2}} \leq 1. \tag{13}$$

3.2 *MBMF Performance*

To evaluate the performance of the MBMF receiver two extreme cases need to be considered as references.

Optimum receiver: If the Green's function were known exactly, i.e. $\mathcal{G}'(\omega,\mathbf{r}) = G'(\omega,\mathbf{r})$, $\forall\omega \in \Omega$, then

$$\rho(\mathbf{r}) = \rho_{\max}(\mathbf{r}), \tag{14}$$

and the MBMF is the optimum receiver,

$$\mathcal{O}(\omega,\mathbf{r}) = \mathcal{O}_0 G'^*(\omega,\mathbf{r})S^*(\omega)\exp(-j\omega\tau). \tag{15}$$

The receiver yields a higher output peak SNR for the received signal shape than for any other signal shape with the same energy.

MF receiver: If the Green's function were totally unknown, i.e. $\mathcal{G}'(\omega,\mathbf{r}) = 1$, $\forall\omega \in \Omega$, then

$$\rho(\mathbf{r}) = \frac{2\mathcal{E}_s}{N_0}\alpha(\mathbf{r}) \equiv \rho_0(\mathbf{r}), \tag{16}$$

where

$$\alpha(\mathbf{r}) \equiv \max_{\xi} \left| \frac{1}{\Delta\omega} \int_{\Omega} G'(\omega, \mathbf{r}) \exp(j\omega\xi) d\omega \right|^2 . \tag{17}$$

The receiver is the conventional matched filter (MF),

$$H(\omega, \mathbf{r}) = H_0 S^*(\omega) \exp(-j\omega\tau). \tag{18}$$

The reduction of peak SNR at the MF output due to energy time spreading is quantified by the ratio

$$\frac{\rho_0(\mathbf{r})}{\rho_{\max}(\mathbf{r})} = \frac{\alpha(\mathbf{r})}{\beta(\mathbf{r})} = \gamma(\mathbf{r}) \leq 1. \tag{19}$$

where

$$\gamma(\mathbf{r}) \equiv \frac{\max_{\xi} \left|\int_{\Omega} G'(\omega, \mathbf{r}) \exp(j\omega\xi) d\omega\right|^2}{\Delta\omega \int_{\Omega} \left|G'(\omega, \mathbf{r})\right|^2 d\omega} \tag{20}$$

Processing gain: The relative performance of the MBMF and MF processing is quantified by the ratio

$$\frac{\rho(\mathbf{r})}{\rho_0(\mathbf{r})} = \frac{\max_{\xi} |\mathcal{R}_{G'\mathcal{G}'}(\xi, \mathbf{r})|^2}{\gamma(\mathbf{r})}. \tag{21}$$

The MBMF processing gain relative to the MF is equal to the degree of time dispersion in the actual channel ($1/\gamma \geq 1$), weighted by the degree of similarity ($0 \leq |\mathcal{R}|^2 \leq 1$) between the actual and modeled channel responses, both evaluated over the frequency band of transmission Ω. The product of these two quantities is not necessarily greater than one. In the event that the medium Green's function is poorly modeled, the MF receiver outperforms the MBMF receiver.

When H and $\mathcal{H}$ are normalized to the same energy, the output noise mean levels are equal and the peak levels can be compared. The arbitrary constants in Eqs. (11) and (18) must satisfy the relation

$$\frac{|\mathcal{H}_0|^2}{|H_0|^2} = \frac{\Delta\omega}{\int_{\Omega} |\mathcal{G}'(\omega, \mathbf{r})|^2 d\omega}. \tag{22}$$

3.3 Space Coherent MBMF Processing

For an arbitrary K-element array the receiver inputs are

$$x_k(t) = r_k(t) + n_k(t) = g_k(t) \otimes s(t) + n_k(t) \tag{23}$$

and the receiver output is defined as the coherent sum

$$y(t) = \sum_{k=1}^{K} y_k(t) = \sum_{k=1}^{K} h_k(t) \otimes x_k(t). \tag{24}$$

where k refers to $\mathbf{r}_k$, the difference in radius vectors between the point source and the kth receiver.

3.4 Definition of Inversion Metrics and Objectives

Objective functions suitable for inversion derive from the MBMF processing gain relative to the MF [Eq. 21]. This metric is called MBMF gain from this point on. We denote $\mathbf{p}$ the model parameter vector and Π the parameter space such that $\mathbf{p} \in \Pi$.

Time coherent: The objective function for a single receiving element is defined as

$$\Phi(\mathbf{r}, \mathbf{p}) \equiv \frac{\phi(\mathbf{r}, \mathbf{p})}{\phi_0(\mathbf{r})}, \quad \Phi > 0, \tag{25}$$

where ϕ and ϕ_0 are the peak levels of the MBMF and MF receiver outputs $y(t)$. ϕ replaces ρ to emphasize that the input signal $x(t)$ and reference signals $h(t)$ of the receivers are normalized to *unit* energy such that

$$0 < \phi \leq 1 \text{ and } 0 < \phi_0 \leq 1. \tag{26}$$

With this normalization ϕ is an estimate of the correlation coefficient between the measured and synthesized band-limited (Ω) impulse responses.

Space-time coherent: The objective function for K receiving elements is defined as

$$\Psi(\mathbf{r}_1, \mathbf{r}_2, \cdots, \mathbf{r}_K, \mathbf{p}) \equiv \frac{\psi(\mathbf{r}_1, \mathbf{r}_2, \cdots, \mathbf{r}_K, \mathbf{p})}{\psi_0(\mathbf{r}_1, \mathbf{r}_2, \cdots, \mathbf{r}_K)}, \quad \Psi > 0. \tag{27}$$

Unit energy normalization is applied to the sum input signal $\sum_k x_k$ and reference signals $\sum_k h_k$ indicated by ψ instead of ρ. Eq. 27 is analogous to the processing gain of a generalized beamformer relative to a plane-wave.

An important attribute of the metrics in Eqs. 25 and 27 is that the magnitude of $1 - \phi$ and the sign and magnitude of $\Phi - 1$ represent the knowledge incorporated in the hypothesized environment. Clearly maximizing ϕ and Φ are equivalent. However, in searching Π, $\mathbf{p}$ solutions for which $\Phi \leq 1$ are excluded (or penalized in an optimization algorithm) and $\mathbf{p}$ solutions for which $\Phi > 1$ are weighted according to Φ magnitude. When ϕ and Φ are expressed in dB, i.e. $20 \log_{10}(\cdot)$, 0 dB is the reference level.

An alternative formulation of the objective is

$$\Upsilon(\mathbf{r}, \mathbf{p}) \equiv \frac{\phi^2(\mathbf{r}, \mathbf{p})}{\phi_0(\mathbf{r})}, \quad \Upsilon > 0, \tag{28}$$

which weights the MBMF gain relative to the MF receiver by the loss relative to the optimum receiver $(\phi < 1)$.

Space incoherent: The overall performance of single-receiver inversion was measured by the quadratic means

$$\overline{\phi} = \sqrt{\langle \phi_k^2 \rangle} \text{ and } \overline{\Phi} = \sqrt{\langle \Phi_k^2 \rangle}, \;\; k = 1, 2, \cdots, 32, \tag{29}$$

where ϕ_k and Φ_k refer to the kth element of the VA. In contrast to Eq. 27 the received signals are weighted equally at all depths independently of their energy. This metric is conservative. When considered as an objective, the matching criterion is more stringent than with Ψ, as shown later.

4

Inversion Approach

4.1 Parametric Search and Optimization

To assess the true performance of MBMF inversion, the environmental parameters were first searched exhaustively. Standard optimization algorithms do not provide statistics of the solutions.

In narrow-band MFP inversion approaches, combinatorial searches have been commonly applied to find a global maximum of an objective (Bartlett power at a single frequency) without being trapped in local minima [7, 9]. As broad-band approaches lead to well-behaved objectives, supervised searches and state-of-the-art nonlinear optimization methods were investigated at the end of this paper.

For very large parameter spaces, a global search based on simulated annealing [40] or genetic [41] algorithms can incorporate the MBMF processor and objective function. Our experience has been that inversion of at-sea data requires physical insight and supervised trial-and-error experiments rather than extensive modeling. Once the inversion model was properly parameterized, constrained nonlinear optimization algorithms were found reliable and more efficient, as shown later.

4.2 Range Dependence Consideration

Even the mild range dependence of the environment presented some difficulty. The thermocline depth and clay layer thickness variability (Table II in [13]) limited the resolution achievable with a RI inversion model. Clearly, solving for a totally unknown RD situation was not feasible with limited computing power. *A priori* knowledge from archival environmental databases and *in situ* measurements were available to support the inversion. Towed oscillating CTD [42] and satellite-sensed sea surface temperature data provided detailed ocean sound speed cross-sections of transect XF. Bathymetry and bottom stratigraphy were derived from high-resolution echo sounding and sediment profiling, respectively.

Range-independent (RI) and range-dependent (RD) inversions were performed. For RD inversion, the 2-D ocean SSP, bathymetry and stratigraphy measured *in situ* were included in the model (Fig. 2). The clay layer thickness variation was calculated from seismic two-way travel times and depth-average sound speed. The calculation was biased as the clay SSP was not known *prior* to RD inversion. However the bias was negligible in comparison with the thickness variation (5–9 m) with range. For RI inversion, ocean SSP and bathymetry were averaged over range.

4.3 *Inversion Model Parameterization*

The bottom inversion model was defined as a sediment layer and a half-space homogeneous bottom, referred to as clay layer and silt bottom. The parameter space, discretization steps and bounds are given in Table 2. For both RI and RD inversions the following assumptions and parameterization were made. 1) Known densities (ρ) of the clay layer and silt bottom were held fixed. 2) Unknown attenuations (β) of the clay layer and silt bottom were varied. 3) Unknown compressional wave sound speed (c_p) profile in the clay layer was modeled by a top c_p at the water-bottom interface and a semi-positive gradient (∂c_p) both constant with range, and varied. 4) Unknown c_p of the silt bottom was constant with depth and range, and varied. 5) c_p at the bottom of the clay layer was constrained to be greater than the silt. 6) Known geometric parameters (z_s, z_r and R) of the experimental setup were held fixed. Six geoacoustic parameters were searched exhaustively. In addition the clay and silt ρ and β were searched locally about the maximum. Inversion models are designated as RIR and RDR where R is the range rounded to the kilometer.

4.4 *Green's Function Synthesis*

Medium Green's functions $\mathcal{G}(t, \mathbf{r}, \mathbf{p})$ were Fourier synthesized from 104 CW complex pressure solutions with a frequency spacing $\delta f = 5.859375$ Hz over the frequency band $\Omega = [199.218750, 802.734375]$ Hz. These values correspond to a discrete Fourier transform (DFT) with sampling frequency $f_\mathrm{s} = 6000$ Hz and length $N = 1024$ ($\Delta T = N/f_\mathrm{s} = 170.667$ ms). From Nyquist sampling theorem the frequency spacing δf was constrained by the inequality $\delta f \leq 1/D$ where D is the total time dispersion, i.e. the difference in group delay between the slowest and fastest modes over the whole frequency band for every candidate environment. The CW solutions were calculated with modified versions of acoustic propagation models [43]: the normal mode model SNAP [44] for RI environments, and the coupled normal mode model C-SNAP [45]) with a range spacing $\delta R = 50$ m for RD environments. Adiabatic approximation was not sufficient for the 6–15 km part of the transect where sharper variations of bathymetry and clay layer thickness (Fig. 5) caused mode coupling.

Table 2 *RI and RD inversion models for Yellow Shark transect XF*

Model parameter	p	Run	p_l	δp	p_u	#
Geometric						
source depth	z_s (m)		known			
receiver depths	z_r (m)		known			
range	R (km)		known			
Water column						
density	ρ_water		1			
depth	z_water (m)	RI	$\langle z_\mathrm{water}\rangle_R$			
		RD	$z_\mathrm{water}(r)$			
sound speed	c_water (m/s)	RI	$\langle c_\mathrm{water}(z)\rangle_R$			
		RD	$c_\mathrm{water}(z,r)$			
Clay layer						
density	ρ_clay		1.5			◇
		RI	1	0.1	2.5	16
attenuation	β_clay (dB/λ)	RI	0.04	0.02	0.08	3
			0.01	0.01	0.2	20
		RD	0.06			◇
sound speed	c_clay (m/s)	RI	1450	5	1510	13
			1400	5	1500	21
		RD	1400	5	1540	29
gradient	∂c_clay (s^{-1})	RI	0	1	5	6
			0			◇
		RD	0	0.5	10	21
thickness	Δz_clay (m)	RI	0	0.5	10	21
		RD	$\Delta z_\mathrm{clay}(r)$			
Silt bottom						
density	ρ_silt		1.8			◇
		RI	1	0.1	2.5	16
attenuation	β_silt (dB/λ)	RI	0.1	0.05	0.2	3
			0.05	0.05	1	20
		RD	0.15			◇
sound speed	c_silt (m/s)	RI	1520	10	1600	9
		RD	1540			◇

$\mathbf{p} = [\rho_\mathrm{clay}, \beta_\mathrm{clay}, c_\mathrm{clay}, \partial c_\mathrm{clay}, \Delta z_\mathrm{clay}, \rho_\mathrm{silt}, \beta_\mathrm{silt}, c_\mathrm{silt}]$ is the model vector. The densities ρ are ratios referenced to water. The ◇ symbol indicates fixed parameter value. Models are designated RIR or RDR where R is the range rounded to the kilometer.

4.5 Acoustic Data Processing

The VA received signals $x_k(t)$, $k = 1, 2, \cdots, 32$, were matched-filtered with the transmitted signal $s(t)$ (MF) and received signals synthesized for every candidate environment $r_k(t, \mathbf{p}) = g_k(t, \mathbf{p}) \otimes s(t)$ (MBMF). The signals measured by the source reference hydrophone were used for $s(t)$ to compensate for distortion in the transmission chain (amplifiers and acoustic projectors). The peak levels in Eqs. 25 and 27 were determined from the envelopes of the single or summed receiver outputs,

$$\phi(\mathbf{p}) = \max_t |y(t, \mathbf{p})| \text{ and } \phi_0 = \max_t |y_0(t)| \tag{30}$$

where $|\cdot|$ denotes the magnitude of the corresponding analytic (complex-valued) signal calculated via Hilbert transform.

4.6 Pings Selected for Inversion

The reproducibility of the waveguide impulse response measurements at each range (Fig. 3) justifies the use of any single ping to represent the ensemble of pings, for the purpose of bottom inversion. Fig. 6 shows the MF real-valued outputs for the selected pings (Table 1). On 10 September 1994 the selected pings correspond to the mid point of the 9 km and 15 km oceanographic runs, i.e., when the measured 2-D sound speed profile used in the inversion models best represented the intervening one (Fig. 5 in [13]). On 11 September the 4.5 km and 6 km acoustic runs were delayed with respect to the oceanographic runs so that the first ping from each run was used for the inversion.

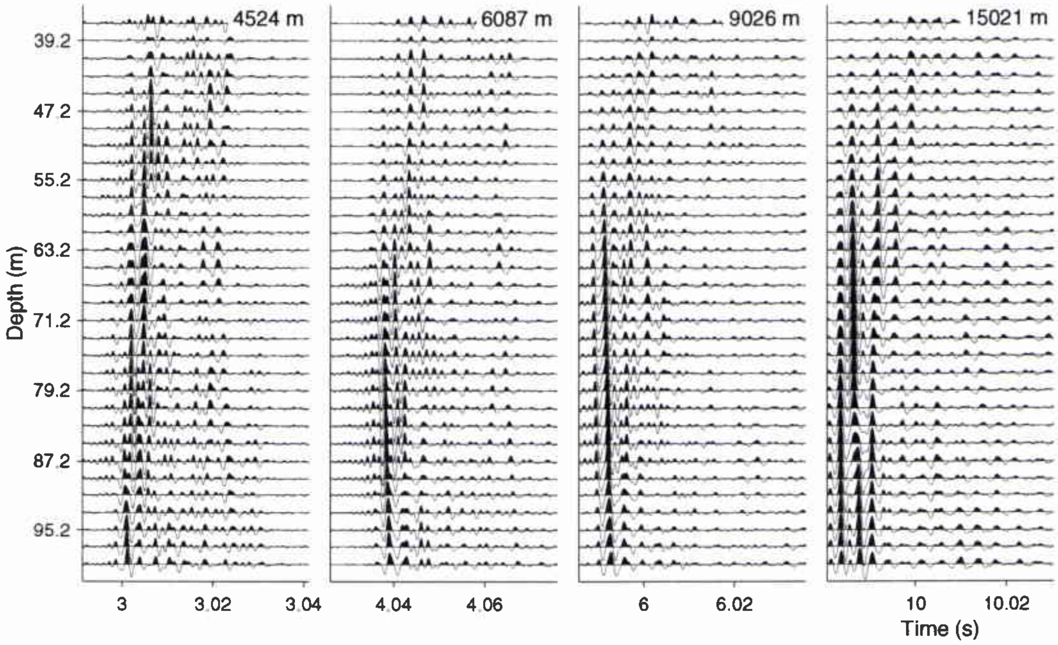

Figure 6 *Waveguide impulse response measurements selected for inversion at the four ranges: (a) 4.5 km, 11 September 1994 1318 UTC ping, (b) 6 km, 11 September 1994 0732 UTC ping, (c) 9 km, 10 September 1994 1808 UTC ping, (d) 15 km, 10 September 1994 1050 UTC ping.*

5

Experimental Inversion Results

Single-depth and space-coherent MBMF inversion runs were performed from signals transmitted at 4 ranges and received at 32 depths, with both RI and RD models. Due to space limitations, results are presented graphically for inversion runs with 9 km data only. Other runs including data-oriented simulations are discussed.

5.1 Propagation over a Soft Sediment Layer

The propagation over a slow bottom layer is characterized by narrow bands of high TL the central frequencies of which are analytically related to the ratios $c_{\text{clay}}/c_{\text{water}}$, $c_{\text{clay}}/c_{\text{silt}}$, and $\rho_{\text{silt}}/\rho_{\text{clay}}$, and Δz_{clay} [46]. As frequency increases, waterborne modes, in increasing numerical order, begin to travel only in the lossy slow sediment layer with concomitant increased attenuation and decreased group velocity [Fig. 2(c) in [30]]. The transition frequency associated to each mode corresponds to a propagation null.

5.2 Modal Dispersion and Attenuation

For nominal conditions of transect XF, i.e. $\rho_{\text{clay}} = 1.5$, $c_{\text{clay}} = 1485$ m/s, $\Delta z_{\text{clay}} = 8$ m and $c_{\text{silt}} = 1540$ m/s, the first three "null" frequencies are $f_1 = 130$ Hz, $f_2 = 663$ Hz and $f_3 = 1196$ Hz. Mode 1 is mostly contained in the clay layer, and in the water column, is strongly attenuated over the frequency band of transmission $\Omega = [200, 800]$ Hz. Mode 2 is waterborne for $f < f_2$, and sediment borne for $f > f_2$. The higher-order modes are waterborne as $f < f_m \; \forall m \geq 3$ and $\forall f \in \Omega$.

Fig. 7 shows the amplitude distribution in time and depth of all modes summed coherently, and of modes 2–5 taken separately, for a range of 9 km. The high-loss mode 1 is not shown. Modes 2 and 3 are the most energetic with significant intermodal dispersion (a few ms). In the upper third of the waveguide, high-order (≥ 4) modes are dominant. Intramodal dispersion increases with mode order. Mode filtering and interference produce a depth-dependent arrival structure characteristic of the bottom conditions. Even small changes of the bottom SSP have a profound effect on the broad-band mode pattern and arrival structure at a single arbitrary

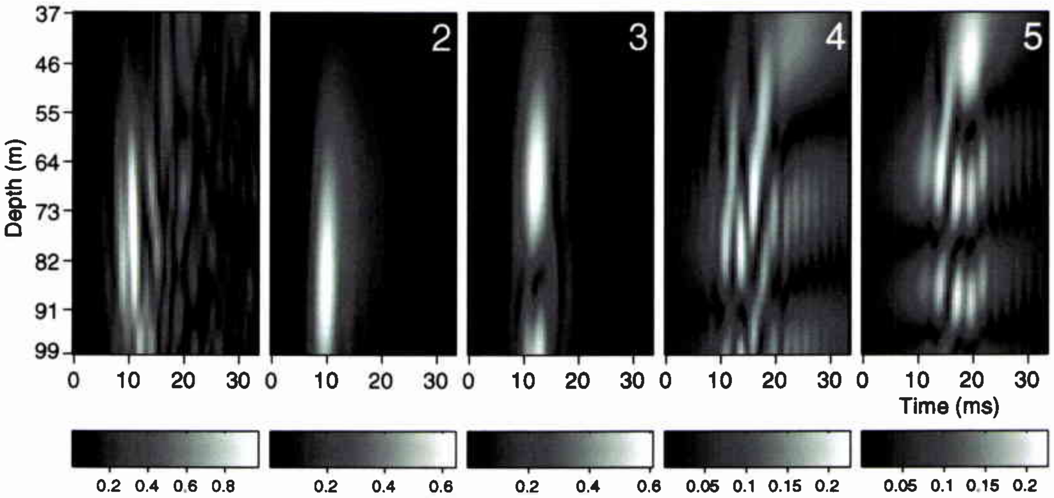

Figure 7 *Modeling of the spatiotemporal structure of the wavefield, and modal dispersion and attenuation over a slow bottom layer: coherent sum (left) and individual modes (2–5).* $R = 9$ *km,* $\Omega = [200, 800]$ *Hz,* $\rho_{\text{clay}} = 1.5$*,* $c_{\text{clay}} = 1485$ *m/s,* $\Delta z_{\text{clay}} = 8$ *m and* $c_{\text{silt}} = 1540$ *m/s.*

depth [25]. It is noted from the mode coherent sum in Fig. 7, that the effects of both types of dispersion, i.e. intermodal and intramodal, can be observed at most depths.

5.3 Optimum Receiver Gain and MBMF Sensitivity

For further references, the optimum receiver gain and MBMF receiver sensitivity are evaluated for the experimental conditions (Fig. 2).

Soft sediment layer: Fig. 8 shows the optimum receiver gain Φ_k *versus* depth for soft top sediment layers of different sound speeds and thickness overlying a harder bottom, for a range of 9 km. There is an overall increase of Φ_k with bottom softness, i.e. for $c_{\text{clay}} \to 1400$ m/s and $\Delta z_{\text{clay}} \to 10$ m. The detailed features can be explained from modal analysis.

When c_{clay} varies [Fig. 8(a)], Φ_k increases at the depths where dispersed modes contribute significantly to the wavefield. A water depth interval of lower Φ_k values is centered about 82 m where one mode only prevails and is weakly dispersed (of order 2 or 3 depending on c_{clay} value, $f_2 = 291$ Hz and $f_3 = 544$ Hz for $c_{\text{clay}} = 1400$ m/s).

When Δz_{clay} increases [Fig. 8(b)], the frequency components of mode 1 and then mode 2 enter progressively the sediment layer, while the higher-order modes become

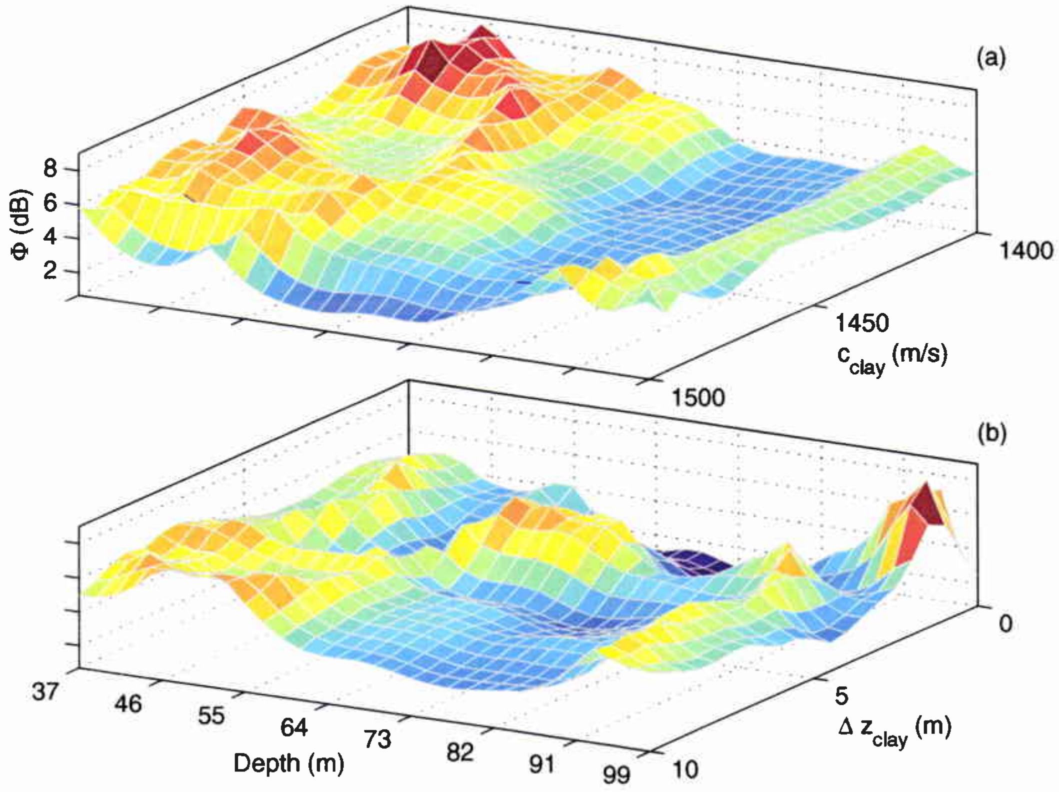

Figure 8 *Optimum receiver gain* versus *depth for varying soft bottom parameters: (a)* c_{clay} *with* $\Delta z_{\text{clay}} = 8$ *m and (b)* Δz_{clay} *with* $c_{\text{clay}} = 1485$ *m/s.* $R = 9$ *km,* $\Omega = [200, 800]$ *Hz,* $\rho_{\text{clay}} = 1.5$, $\beta_{\text{clay}} = 0.06$ dB/λ, $c_{\text{clay}} = [1400, 5, 1500]$ *m/s,* $\Delta z_{\text{clay}} = [0, 0.5, 10]$ *m,* $\rho_{\text{silt}} = 1.8$, $\beta_{\text{silt}} = 0.15$ dB/λ, *and* $c_{\text{silt}} = 1540$ *m/s.*

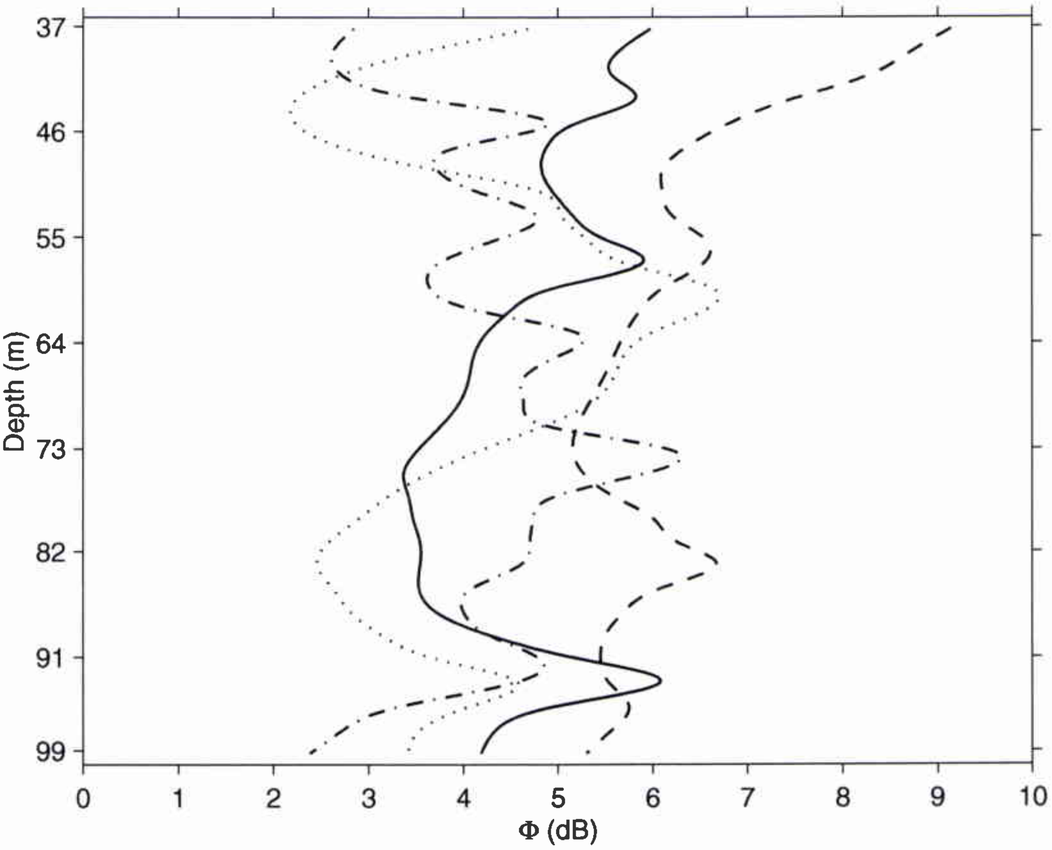

Figure 9 *Optimum receiver gain* versus *depth at different ranges:* $R = 4.5$ *km (dash-dot),* $R = 6$ *km (dot),* $R = 9$ *km (solid) and* $R = 15$ *km (dash).* $c_{\text{clay}} = 1485$ *m/s and* $\Delta z_{\text{clay}} = 8$ *m. Other parameter values are the same as Fig. 8*

more dispersed, resulting in higher Φ_k values towards the waveguide boundaries. Two distinct peaks are related to mode 1 filtering [$f_1 = \max(\Omega) = 800$ Hz for $\Delta z_{\text{clay}} = 1.3$ m and $f_1 = \min(\Omega) = 200$ Hz for $\Delta z_{\text{clay}} = 5.2$ m].

Range dependence: Fig. 9 shows the optimum receiver gain Φ_k *versus* depth for the four transmission ranges, and for $c_{\text{clay}} = 1485$ m/s and $\Delta z_{\text{clay}} = 8$ m. The depth variations of Φ_k become smoother with range as a result of depletion of interfering modes. The intramodal part of dispersion takes over the intermodal part, and the effects of mode filtering by the secondary low-speed waveguide develop with range. There is marked increase of Φ_k near the waveguide boundaries because of the larger contribution of time-dispersed high-order modes. These predictions with a simple bottom model correspond qualitatively to the measured energy time spread in Fig. 4.

Sensitivity: Fig. 10 shows the sensitivity of the MBMF gain to varying two clay parameters. The reference environment is for $c_{\text{clay}} = 1485$ m/s and $\Delta z_{\text{clay}} = 8$ m.

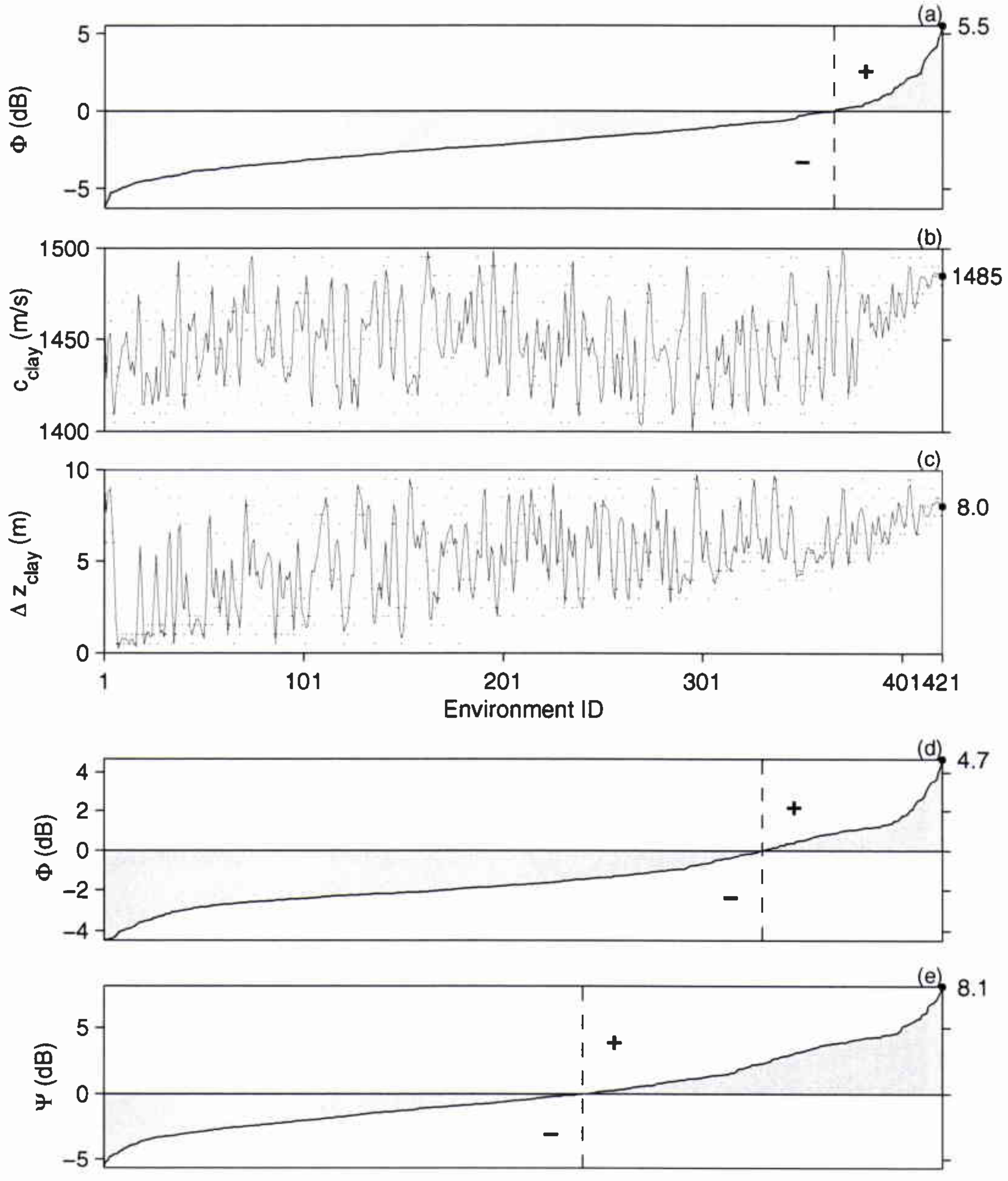

Figure 10 *Sensitivity of MBMF gain to varying soft bottom parameters: (a) Magnitude-sorted objective* Φ_k *at 55.2 m depth and corresponding (b)* c_{clay} *and (c)* Δz_{clay} *values (dots) and non-linear running medians [47] (solid); (d) depth-average* $\overline{\Phi}$ *and (e) space-coherent* Ψ. $R = 9$ *km,* $\Omega = [200, 800]$ *Hz,* $\rho_{\text{clay}} = 1.5$, $\beta_{\text{clay}} = 0.06$ dB/λ, $c_{\text{clay}} = [1400, 5, 1500]$ *m/s,* $\Delta z_{\text{clay}} = [0, 0.5, 10]$ *m,* $\rho_{\text{silt}} = 1.8$, $\beta_{\text{silt}} = 0.15$ dB/λ, *and* $c_{\text{silt}} = 1540$ *m/s.*

The Φ_k, $\overline{\Phi}$ and Ψ objectives were sorted in ascending order of magnitude. The single-depth objective Φ_k exhibits high sensitivity [Fig. 10(a)]. Only about 10% of the parameter combinations yields a positive MBMF gain. The trend and variation of the sorted parameters are related to the objective sign and magnitude [Figs. 10(b) and (c)]. Comparison of the 0 dB crossing-point abscissae shows that the space-coherent objective Ψ is less sensitive to mismatch than single-depth Φ_k and depth-average $\overline{\Phi}$ [Figs. 10(d) and (e)]. The sensitivity of Φ_k was depth dependent and at most depths, higher than Ψ.

Other modeled objectives showed similar sensitivity to silt sound speed but lower sensitivity to clay sound speed gradient and to clay and silt densities and attenuations as will be seen from at-sea data.

Hard vs soft bottom: The potential of MBMF is not limited to inversion of soft bottoms. Fig. 11 shows the optimum receiver gain Φ_k *versus* depth for hard bottoms of different sound speeds (c_p). Achievable gains are of the same order as for a soft top layer and decrease as $c_\mathrm{p} \rightarrow c_\mathrm{water}$. Here, the depth distribution is independent of c_p. Larger values are spread over the downward refracting part of the SSP (Fig. 2) as for the soft bottom case, and are strongly localized in depth (95 m) close to the sea floor.

Optimum spatial sampling: To some extent, suitable depths for transmission and reception can be choosen *a priori*. It will be evident later that the depths at which the optimum receiver gain is greater are generally better in resolving the environment. For hard bottom type, suitable reception depths can be determined from range-averaged water depth and SSP [e.g. Fig. 11]. For soft bottom type, these depths are not as well determined as the thickness and to a lesser extent the sound speed, of the top sediment layer have an effect upon the frequency-dependent modal functions [e.g. Fig. 8]. In the major part of the water column the "optimum depths" are determined by the sound speed gradient structure and near the sea floor, by the bottom acoustic penetration.

The source/receiver geometry should be chosen such that, in the measurements, the effects of bottom interaction are maximized and ocean variability minimized. SNR (TL *versus* ambient noise) and signal time coherence (decorrelation due to medium inhomogeneities) are depth dependent. Signals received close to the sea floor are typically less affected by near-surface ocean variability (e.g. Fig. 3). In these respects, downward refracting conditions with source and receiver in the lower part of the waveguide are more favorable.

In principle, the broad-band measurements integrate the bottom conditions over range. However, in a range-dependent situation, the parameter integrals obtained with a RI inversion model can be overly weighted by the conditions local to the receiver. This is due to mode coupling and relates to the depth dependence of the

Report no. changed (Mar 2006): SM-359-UU

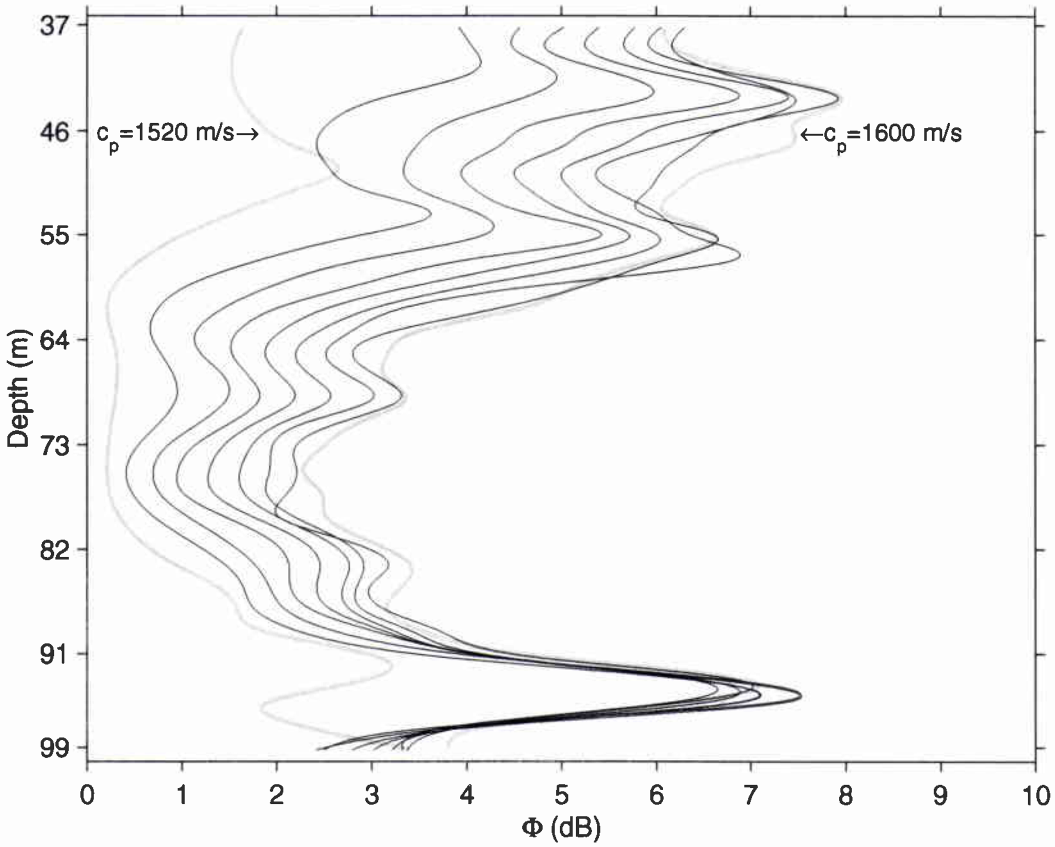

Figure 11 *Optimum receiver gain* versus *depth for hard bottoms. The sound speed* c_{p} *increases from left (dot) to right (solid).* $\Omega = [200, 800]$ *Hz,* $R = 9$ *km,* $\rho = 1.8$, $\beta = 0.15$ dB$/\lambda$, *and* $c_{\mathrm{p}} = [1520, 10, 1600]$ *m/s.*

relative contribution of local low and high order mode functions to the waveform received at a single depth.

5.4 Model-Based Inversion

The bottom properties of the transect XF were first determined by varying systematically the values of six geoacoustic parameters within the bounds defined in Table 2.

Fig. 12 compares the MF output with the MBMF output for RI9 replicas that best matched the signals received on the VA from the sound source at 9 km range. For both space-coherent (a) and single-depth (b) MBMF processing, most of the energy spread in time was recombined coherently into a single peak with more than ten (+11.2 dB) and three (+5.0 dB) times the energy respectively. The respective estimated losses relative to the optimum receiver (unit energy) are small (−1.9 dB and −1.6 dB). The single-depth MBMF gains compared well with the predicted optimum receiver gains (solid line in Fig. 9).

The high degree of time symmetry of the single-depth MBMF envelope outputs indicate that the MBMF replicas closely modeled the received signals. The corresponding real-valued outputs are good estimates of the received autocorrelation functions. The time resolution, i.e. the width of the main peak, is inversely proportional to the effective bandwidth (Eq. 34 in [27]) of the received signal which is smaller than the transmit because of attenuation of certain spectral components ($1/\Delta f = 2.4$ ms *versus* 1.7 ms between the -3 dB points). The effective bandwidth and hence the time resolution, varied with depth. In the present situation, depth-dependent narrow frequency bands of high TL occured as a result of the soft top sediment layer [30, 31]. The sidelobes have a level comparable to the sinc function (−13 dB).

5.5 MBMF Performance versus Depth

Fig. 13 shows the single-element objectives ϕ_k and Φ_k *versus* depth from the trials of over 10^5 RI9 candidate environments ($\mathbf{p}$ values). The environments were ranked in ascending order of objective magnitude.

In Fig. 13(a) the MBMF peak levels, which represent the correlation coefficient between actual and predicted responses, attain acceptable values at all depths ($\phi_k > 0.78, \forall k$). The data are matched unevenly over depth. The coefficients are closer to unity ($\phi_k > 0.9$) in the lower two thirds of the waveguide, where more (+3 dB) energy is received [solid line in Fig. 4(a)]. The slightly poorer match in the upper third is due

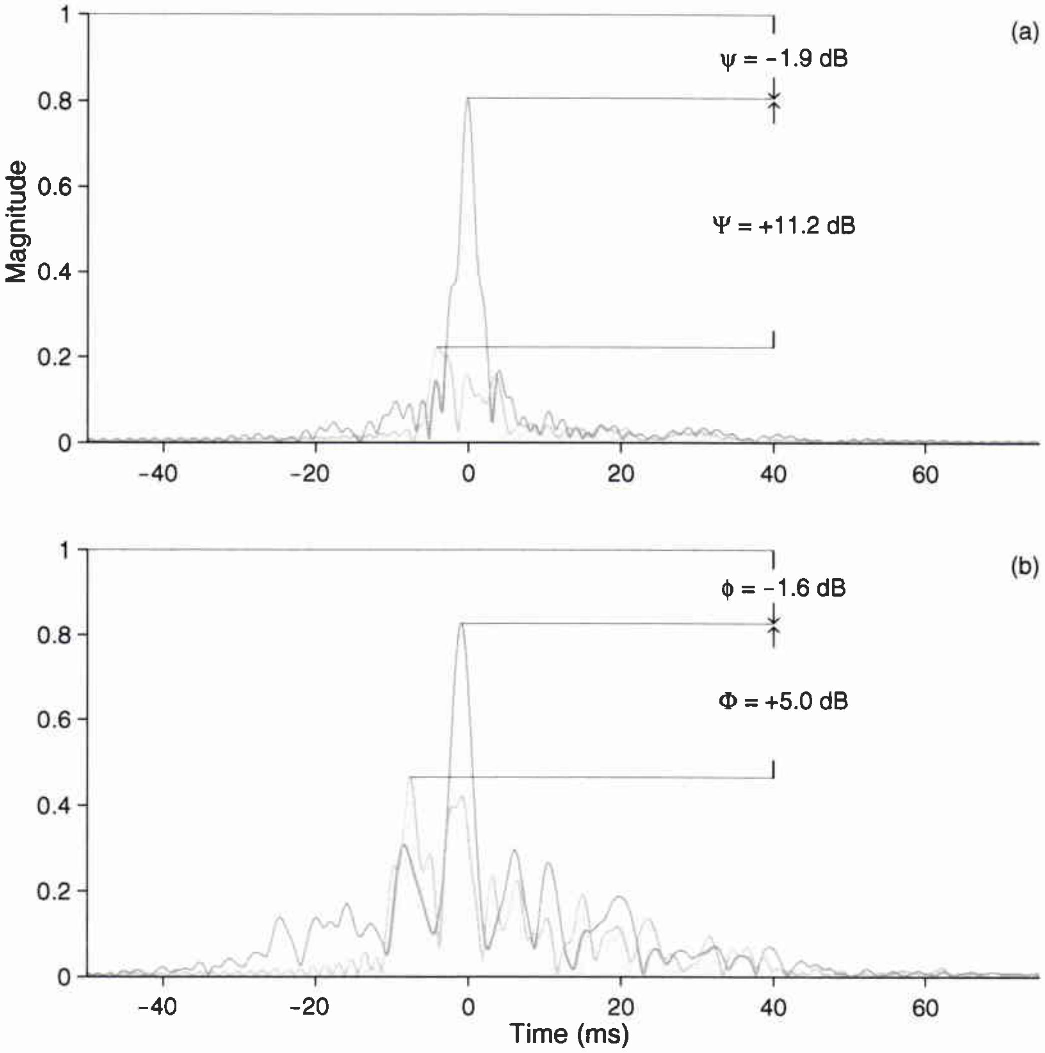

Figure 12 *Comparison of MF (gray filled) and MBMF (solid) envelope outputs for the RI9 bottom model parameters that maximized the objective* Ψ*: (a) space-coherent processing of the 32 VA signals (*Ψ*) and (b) processing of a single VA signal at 55.2 m water depth (*Φ*). The MBMF gain relative to the MF receiver and loss relative to the optimum are indicated.*

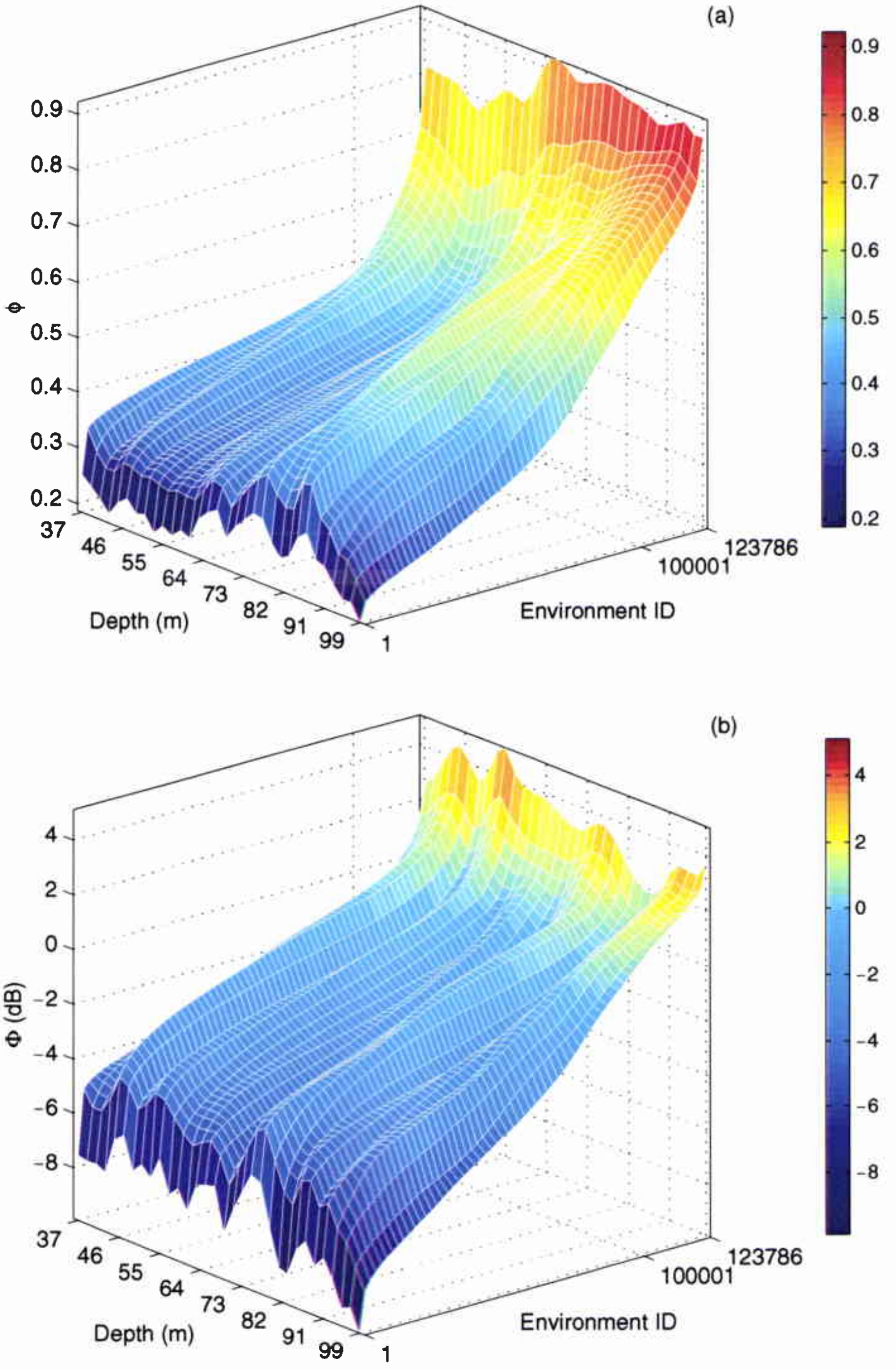

Figure 13 *Sensitivity of the objectives ϕ_k (a) and Φ_k expressed in dB (b)* versus *depth for RI9 inversion. Varied parameters are β_{clay}, c_{clay}, ∂c_{clay}, Δz_{clay}, β_{silt} and c_{silt}. The 123786 tested environments were sorted in ascending order of objective magnitude.*

to the combined effects of lower SNR, decreased signal coherence and the complex arrival structure (Fig. 3) which was not fully modeled using a RI approximation.

In Fig. 13(b) the MBMF gains relative to MF attain positive values at all depths ($\Phi_k > 2$ dB). Environmental match results in higher MBMF gains (up to +5 dB) at the depths where the measured energy time spreading was stronger [solid line in Fig. 4(b)]. This depth dependence was anticipated in the prediction of the optimum receiver gain for a simplified bottom model [solid line in Fig. 9]. Mismatch results in the highest loss (down to −10 dB) very near the bottom.

The surfaces in Fig. 13 represent the objective sensitivity to bottom properties to the exclusion of other known experimental conditions which were incorporated into the modeling. The bottom is not resolved equally at all depths. The overall resolution in parameter vector $\mathbf{p}$ is determined by the objective gradients $\partial\phi_k/\partial\mathbf{p}$ and $\partial\Phi_k/\partial\mathbf{p}$. The gradients remain relatively constant in most of the negative MBMF gain region, then increase rapidly in the positive region for most depths. Along the loci of maxima, the gradients decrease with depth. The better resolution at upper depths is due to the greater complexity of the local field, which conveys more information. The larger gradients of ϕ_k and Φ_k correspond to the larger magnitudes of Φ_k. This confirmed the adequacy of optimum receiver gain prediction in selecting suitable reception depths as discussed earlier. In a corresponding simulated case, $\phi_k \rightarrow 1$ irrespective of depth, but the depth dependence of ϕ_k and Φ_k sensitivities to $\mathbf{p}$ mismatch were similar as in the real data case.

5.6 Bottom Parameter Ambiguity and Resolution

For each inversion run, ambiguity diagrams were constructed for all combinations of the P components of model parameter vector $\mathbf{p}$, taken 2 at a time, i.e. $\binom{N}{2} = P!/2(P-2)!$ pairs (6 for $P = 4$, 15 for $P = 6$). Such diagrams are displayed in Figs. 14 and 15 for RI9 inversion. The depth-average MBMF gain $\overline{\Phi}$ [Eq. 29] is shown as being representative of single-element inversion. In Fig. 14 only the pairs comprising the most sensitive parameters, i.e. c_{clay}, ∂c_{clay}, Δz_{clay} and c_{silt}, are displayed showing distinct regions of negative (blue) and positive (green–brown) gains and no local maximum. In each diagram the positive region is characterized by a ridge with one culminating point [max($\overline{\Phi}$), white square]. The nonlinear relationship between the objective and the different bottom parameters are quantified by the degree of curvature. Only the pair ($c_{\text{clay}}, \partial c_{\text{clay}}$) exhibits a linear relationship. It is apparent that the parameter discretization steps were sufficiently small in comparison with the effective resolution.

In Fig. 15, $\overline{\Phi}$ is always positive over the wide range of locally searched density and attenuation values. The density resolution is higher for the clay than for the silt. The MBMF gain which does not account for TL is less sensitive to attenuation.

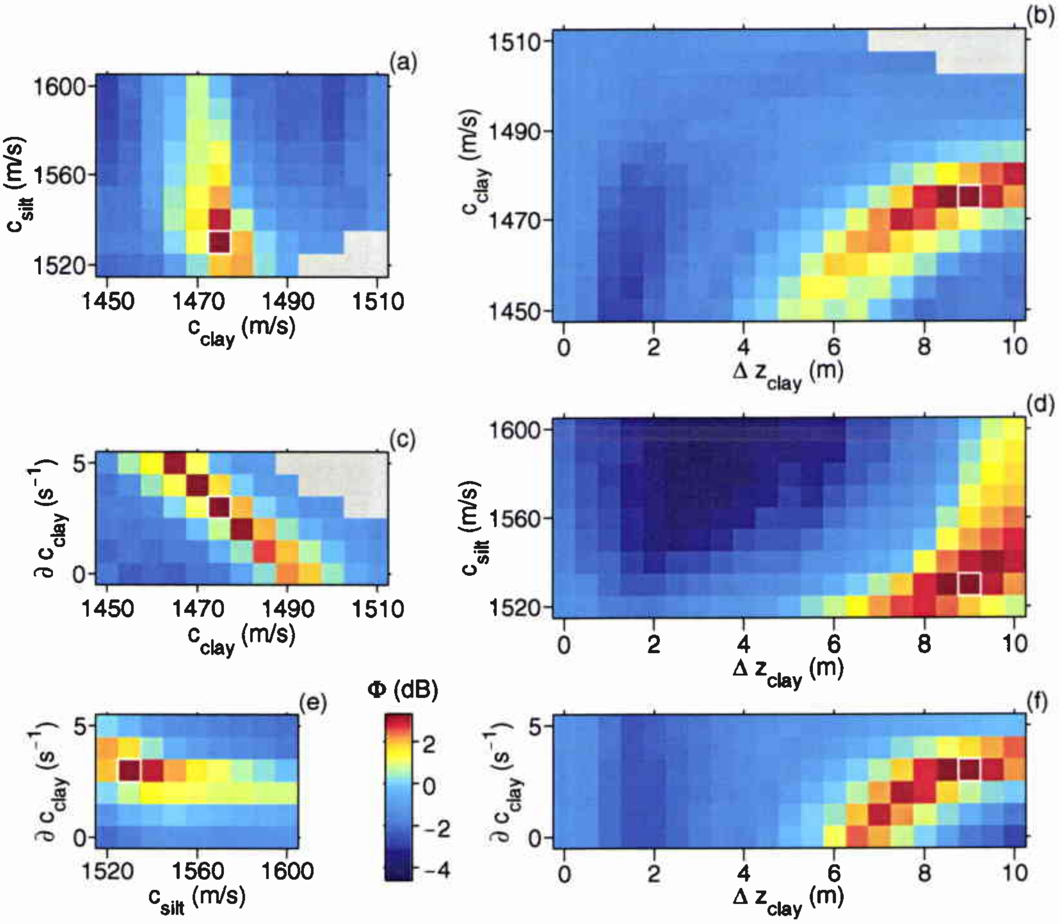

Figure 14 *Ambiguity of RI9 parameters:* c_{clay}, $\partial c_{\mathrm{clay}}$, Δz_{clay} *and* c_{silt}. *The diagrams show sections of the 6-D ambiguity function* $\overline{\Phi}$ *along the main directions at the point where the function is maximum (white square), i.e.* $\overline{\Phi} = 3.2$ *dB for* $\beta_{\mathrm{clay}} = 0.04$ dB/λ, $c_{\mathrm{clay}} = 1475$ *m/s,* $\partial c_{\mathrm{clay}} = 3$ s^{-1}, $\Delta z_{\mathrm{clay}} = 9$ *m,* $\beta_{\mathrm{silt}} = 0.15$ dB/λ *and* $c_{\mathrm{silt}} = 1530$ *m/s. The densities* ρ_{clay} *and* ρ_{silt} *were fixed. The diagrams comprising* β_{clay} *and* β_{silt} *are not shown (see Fig. 15). The axis limits correspond to the search bounds. Pseudocolor scaling spans the range of objective values in the whole 6-D search space. The gray areas are unsearched (or unphysical) combinations.*

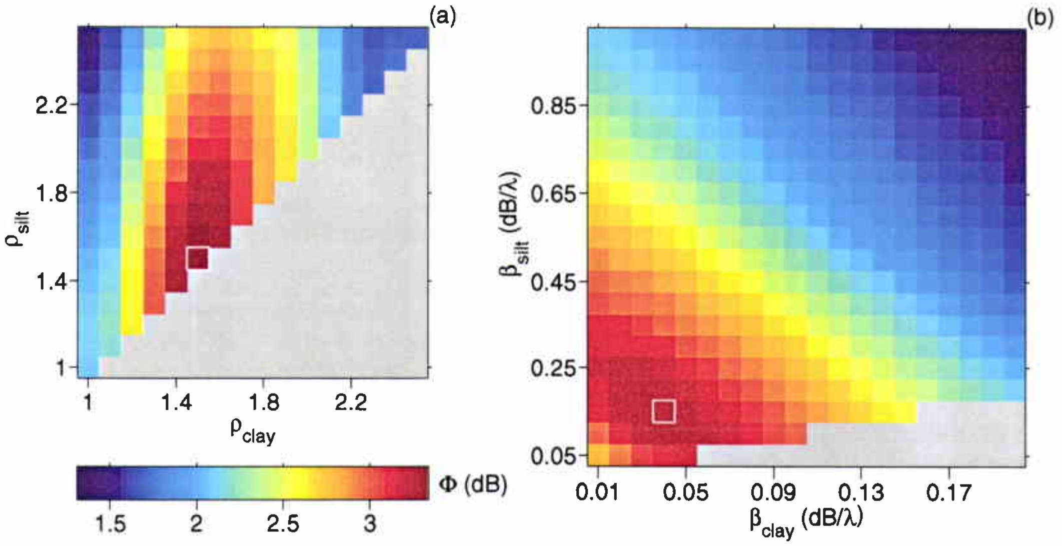

Figure 15 *Ambiguity of RI9 parameters: (a)* $(\rho_{\mathrm{clay}}, \rho_{\mathrm{silt}})$ *and (b)* $(\beta_{\mathrm{clay}}, \beta_{\mathrm{silt}})$ *pairs. The gray areas are the unsearched combinations for which silt values are greater than clay.*

Nevertheless β_{clay} and β_{silt} are resolved as attenuation does not only affect the frequency-dependent received energy (TL), but also its time spreading.

Space-coherent MBMF processing of the 32 VA signals resulted in similar ambiguity properties, but did not enhance resolution because of less stringent matching conditions. This substantiated synthetic-data sensitivity results as shown in Fig. 10. In the objective Ψ [Eq. 27] the lower-energy higher-order mode arrivals, which convey essential information, contribute less to the coherent sum than the main arrivals [Fig. 7]. When compared with single-depth results, the parameter-dependent objective gradients were generally smaller notwithstanding the larger MBMF gains [e.g. Fig. 12(a)].

Fig. 16 compares the $(c_{\mathrm{clay}}, \Delta z_{\mathrm{clay}})$ ambiguity diagrams obtained from Φ_k at the 32 VA depths separately. Only positive gains are displayed for clarity. The clay layer parameters are well resolved at almost every depth. There is definitely no significant solution for which no clay layer exists, i.e. $c_{\mathrm{clay}} \rightarrow c_{\mathrm{silt}}$ and $\Delta z_{\mathrm{clay}} \rightarrow 0$ (upper left region of each diagram). At a few depths, some local maxima occur with MBMF gains which are low relative to the global maximum. Even for a single depth, the broad signaling bandwidth eliminated most of the ambiguity sidelobes commonly observed in narrow-band simulations. Likewise, the depth-dependent ambiguity diagrams for the other parameter pairs resembled their depth averages shown in Fig. 14.

The above at-sea cross-ambiguity results were compared with corresponding mod-

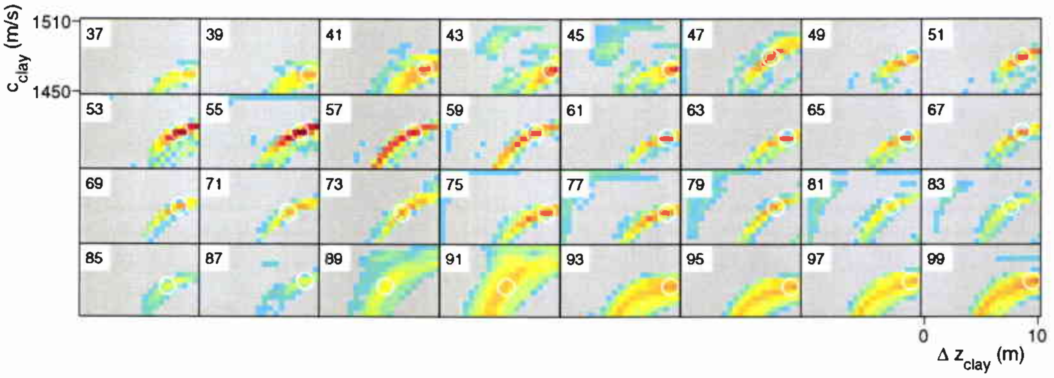

Figure 16 *Depth dependence of the* $(c_{\text{clay}}, \Delta z_{\text{clay}})$ *ambiguity for RI9 single-element inversions. Water depths are indicated in each diagram. Axis limits correspond to search bounds. The pseudocolor scaling spans the range 0–*$\max_{\mathbf{p},k}(\Phi_k)$ *for all diagrams. The combinations for which* $\Phi_k < 0$ *dB are gray-coded.*

eled auto-ambiguity results. The real data were replaced with data synthesized for the parameter values which maximized the real-data objective. The quantitative correspondence between the auto- and cross-ambiguity diagrams indicated that the parameter-dependent resolution was limited by physical observability and not by modeling accuracy.

Examination of the RI4, RI6 and RI15 inversion results showed similar ambiguity and resolution features.

5.7 Objective Statistics

The exhaustive search allowed statistical descriptions of a large set of solutions $\Phi_k(\mathbf{p})$, $\mathbf{p} \in \Pi$. Quantiles of the Φ_k distribution associated to each parameter value were calculated to determine the central tendency of the solutions.

Fig. 17 shows the 90th percentile of the single-depth RI9 objectives. The graphs show the distribution of negative (blue bars) and positive (green bars) $P_{90}(\Phi_k)$, and the maximum $\max(\Phi_k)$ (yellow triangle), for each depth (kth row) and parameter (column). The last row corresponds to $\overline{\Phi}$.

At every depth the correct solution of a "soft layer over hard bottom" is detected with no ambiguity. For c_{clay}, Δz_{clay} and c_{silt} the signed P_{90} distributions are essentially bimodal with their positive part centered about the maximum. The c_{clay}, ∂c_{clay} and Δz_{clay} values that maximized Φ_k vary slightly with depth in a joint and systematic way: a smaller c_{clay} results in larger ∂c_{clay} and Δz_{clay} keeping the c_{clay} average over Δz_{clay} nearly constant. This ambiguity involving three parameters was not

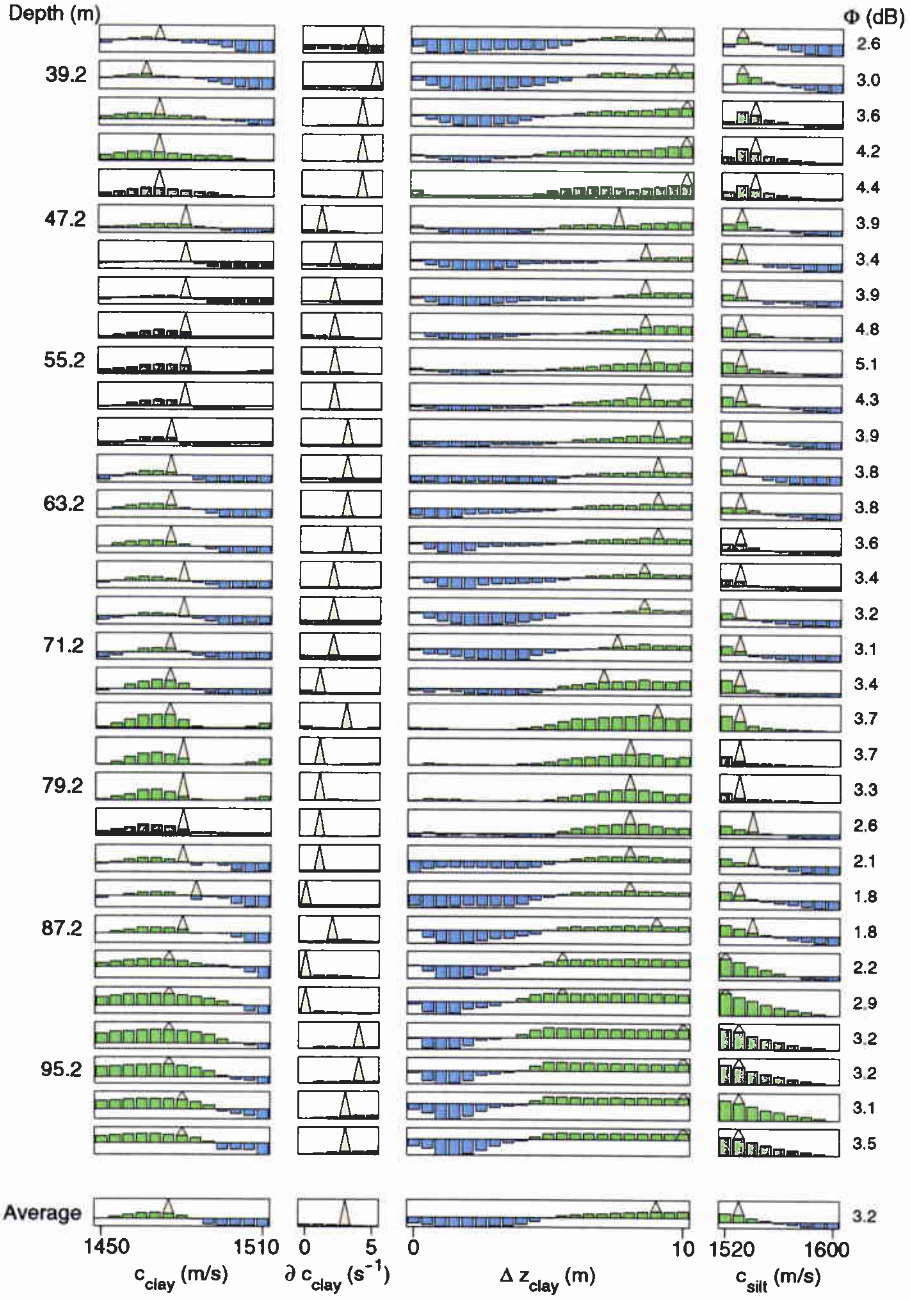

Figure 17 A posteriori *distribution of the objective for single-element RI9 inversions. The four most sensitive parameters (column) are displayed for each of the 32 VA elements (row). Water depths are indicated on the left-hand side. The bottom row corresponds to the depth-average objective* $\overline{\Phi}$*. For each searched value, the 90th percentile* P_{90} *is represented by a blue (MBMF loss) or green (MBMF gain) bar. The horizontal line corresponds to 0 dB (MF). The location (triangle) and value (right-hand side) of* $\max(\Phi_k)$ *are indicated. Each graph is scaled vertically from* $\min[P_{90}(\Phi_k)]$ *to* $\max(\Phi_k)$*. The horizontal axis limits are the search bounds.*

Table 3 *RI9 single-depth versus space-coherent bottom inverses*

		Clay layer				Silt bottom	
	$\Psi,\overline{\Phi}$ (dB)	β_{clay} (dB/λ)	c_{clay} (m/s)	∂c_{clay} (s^{-1})	Δz_{clay} (m)	β_{silt} (dB/λ)	c_{silt} (m/s)
S mean	n/a	*0.048*	*1476.6*	*2.41*	*8.66*	*0.131*	*1531.6*
S m.a.d.	n/a	*0.011*	*3.6*	*1.08*	*0.85*	*0.037*	*4.7*
A	3.2	0.04	1475	3.0	9.0	0.15	1530
C	11.2	0.04	1475	3.0	8.5	0.10	1530

Single-depth (S), depth-average (A) and space-coherent (S) solutions of RI9 inversion runs. For single depth, the mean and mean absolute deviation of the parameter values obtained at the 32 depths separately are given. Fixed parameter values are: $\rho_{\text{clay}} = 1.5$ and $\rho_{\text{silt}} = 1.8$.

apparent in depth-dependent ambiguity diagrams as in Fig. 16. At certain depths the centroid of P_{90} provided more reliable estimates than the max(Φ_k) location (e.g. Δz_{clay} for $z_{\text{r}} = 73.2$ m). Close to the waveguide boundaries the P_{90} distributions for Δz_{clay} flatten and the maxima point to the actual Δz_{clay} local to the VA rather than to the range-averaged Δz_{clay}. This result, confirmed by RD synthetic data/RI inversion, is related to the mode-dependent integrating capability discussed earlier. For ∂c_{clay}, the large differences between the P_{90} and maximum values indicate a sensitivity lower than for the other parameters. The P_{90} distributions for β_{clay} and in particular β_{silt} which appeared uniform over the narrow search window are not shown.

The maxima of the quadratic means of Φ_k such that $\Phi_k \geq 0.95\,\max(\Phi_k)$ were close to $\max(\Phi_k)$.

The well-behaved statistics of Φ_k at most depths gave confidence in the single-hydrophone bottom inverses. Table 3 summarizes the results. The mean of the single-depth results compare well with the depth-average and space-coherent results.

5.8 Comparison with Sediment Core Data

For most depths and ranges, the inverted values of c_{clay}, ∂c_{clay}, Δz_{clay} and c_{silt} represent good piecewise linear fits of the actual range-averaged bottom SSP as best as it can be derived from sediment core and stratigraphic data. In comparing with core data, sediment compaction caused by the liner penetration was taken into account (see Annex A). For example, the core depth in Fig. 24 is less than 70% of the actual depth. Short core data were extrapolated to the thick clay layer conditions of the transect XF as discussed on p. 336 in [13]. The values of β_{clay} and β_{silt} agree with previous broad-band TL data/model comparisons [39] and inversions [31] in the Giglio basin platform. Inclusion of ∂c_{clay} as a variable of the RI model resulted in a small bias on Δz_{clay} at certain depths.

5.9 Comparison with BMFP Bottom Inverses

The performances of BMFP and MBMF inversions can be compared objectively as the respective multitone and broad-band data were acquired under identical experimental conditions. The tones covered the frequency band with third-octave frequencies. For the 9 km range, the *a posteriori* distributions weighted with fitness in Fig. 25 in [13] are comparable to the single-depth P_{90} distributions in Fig. 17. The only differences between the two RI inversion models are that thermocline depth and water depth were varied *versus* fixed and one *versus* two attenuation parameters were varied. The two techniques resolve the bottom, but the maxima are more accurate and the distributions more compact with MBMF than with BMFP. The MBMF, single-hydrophone, bottom inverses were more robust in spite of being derived from 1 *versus* 38 realizations of a 12 s signal.

5.10 Depth Combinations

A hydrophone at a single depth and a VA that spans the water column are two extreme measurement configurations. Intermediate configurations, especially very sparse arrays, are of practical interest.

The space coherent MBMF gain max(Ψ) was calculated for all possible combinations of N VA elements (depths) taken K at a time, i.e.

$$\binom{N}{K} = \frac{N!}{K!(N-K)!} \equiv C(N,K), \;\; K = 1, 2, \cdots, N. \tag{31}$$

For each combination, ϕ and ϕ_0 in Eq. 27 were determined from the coherent sum of the respective single-element MBMF and MF outputs with unit energy normalization depending on the combined elements. The MBMF replicas that maximized Ψ with $N = 32$ VA elements were used.

Fig. 18 shows RI9 results for $N = 16$ elements at 4 m intervals.

In Fig. 18(a) the objectives Ψ, arranged in ascending order of magnitude for each K value, increase at a rate related to the acoustic field complexity. There is an overall increase of Ψ with K, including for the worst combinations. The larger MBMF gains are achieved with fewer elements the depth combinations of which include the more time dispersed signals. The intersection between each (K_1, K_2)

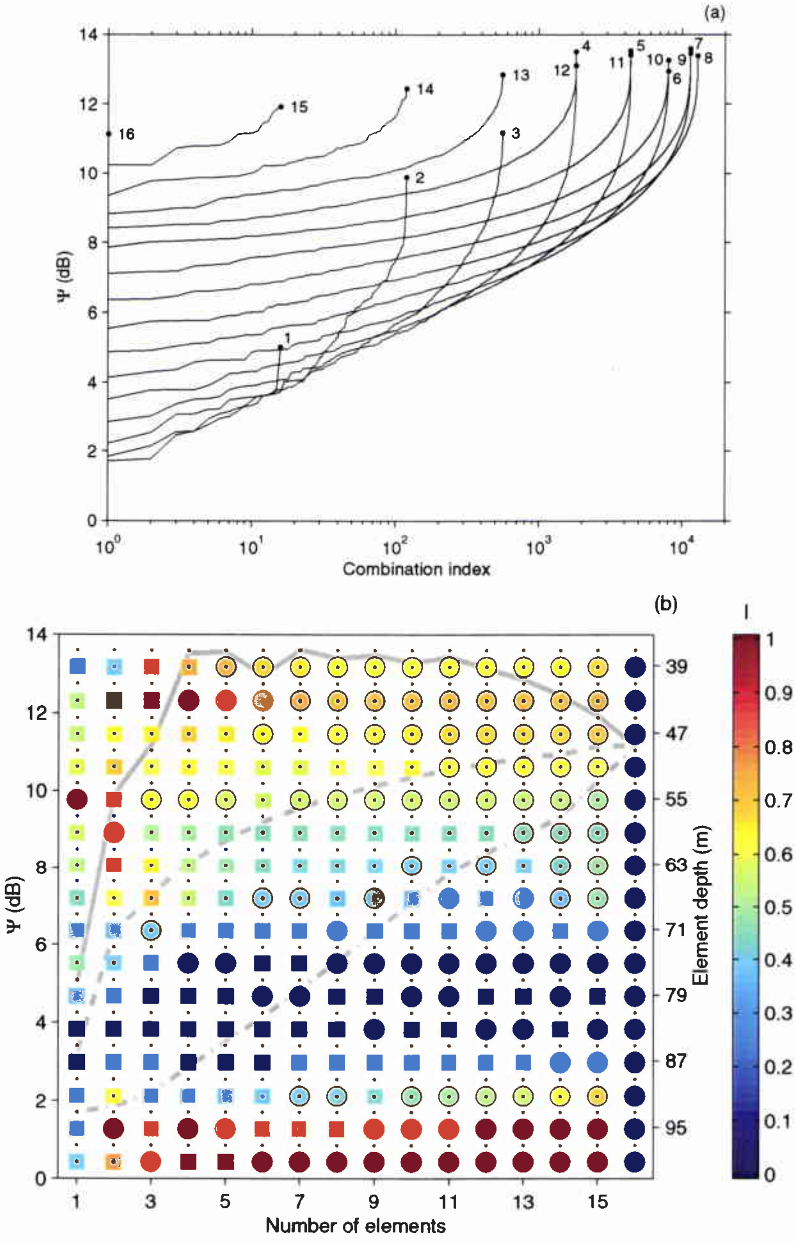

Figure 18 *Space coherent MBMF gain* Ψ *for all possible combinations of* $N = 16$ *VA elements taken* $K = 1, 2, \cdots, N$ *at a time (RI9 inversion). (a) Each curve is the magnitude-sorted* Ψ versus *combination index for each number of elements* K *indicated at the maximum (dot). (b) The three curves (left scale) are the* $\max(\Psi)$ *(solid), median* $P_{50}(\Psi)$ *(dash) and* $\min(\Psi)$ *(dash-dot) calculated from all* K*-combinations [e.g.* $C(16, 8) = 12870$*]. The dots indicate the 32 VA element depths (right scale). The pseudocolor represents the element relative importance* $\mathcal{I}$ *normalized such that* $\min(\mathcal{I}) = 0$ *and* $\max(\mathcal{I}) = 1$ *for* $1 \leq K \leq N - 1$*. The circles in place of the squares indicate the combination that produced* $\max(\Psi)$.

pair of curves determines the relative numbers of K_1 and K_2 combinations, for which $\Psi(K_1) > \Psi(K_2)$ with $K_1 < K_2$. For example, 55% of the 4 element combinations yields a larger MBMF gain than 6% of the 8 element ones. Curves calculated for a corresponding simulated case behaved similarly.

In Fig. 18(b) the relative importance of the elements (colored squares) and the combination that maximizes Ψ (circles) are shown for each K value (vertically). For given K the importance of the kth element relative to N elements is defined as

$$\mathcal{I}(k,K) = \frac{\mathcal{I}' - \min_l(\mathcal{I}')}{\max_l(\mathcal{I}') - \min_l(\mathcal{I}')}, \quad 0 \le \mathcal{I} \le 1, \tag{32}$$

where

$$\mathcal{I}' = \frac{\sum_{\{\, l | \mathbf{c}_l \supset k \,\}} [\Phi(\mathbf{c}_l) - 1]}{\sum_{k=1}^{K} \sum_l [\Phi(\mathbf{c}_l) - 1]}, \quad l = 1, 2, \cdots, C(N,K), \tag{33}$$

and $\mathbf{c}_l$ is the lth combination index vector.

It is instructive to follow, as $K \to N$, how the best (circles) or good (not shown) elements are selected according to $\mathcal{I}$ (color-coded). For $K = 1$ the optimum depth is in the SSP downward refracting part (Fig. 2). For $K = 2$ a second element is added near the sea floor. For $K = 3$ a third element is added between the first two. For $K = 4$ a fourth element is added immediately below the thermocline. As $K \to 16$ additional elements are redistributed over depth and clustered in the boundary regions where $\mathcal{I}$ is higher (yellow–brown). The low (blue–green) $\mathcal{I}$ region spans the 55–85 depths, the energy time spreading of which was smaller [Fig. 4(b)]. The max(Ψ) (solid line), which was obtained with the best combination (circles), increases rapidly to more than 13 dB for $K = 4$ and then decreases slowly to 11 dB for $K = 16$.

A significant gain increase (+5 dB) with respect to $K = 1$ is already achieved with $K = 2$. The median $P_{50}(\Psi)$ (dotted line) increases logarithmically and min(Ψ) (dash-dotted line) *quasi* linearly. In a corresponding simulated case max(Ψ) was also attained with $K = 4$ but increase rates and value for $K = 16$ (7 dB) were smaller than for the real case because there was no intrinsic gain over noise.

Examination of other ranges led to the same observations. At 4.5 km range where the acoustic field comprised a larger number of excited modes max(Ψ) (also 13 dB) was obtained with $K = 6$ elements, but $K = 4$ already yielded 12 dB. For $K > 6$, max(Ψ) decreased more rapidly than for the other ranges.

For complicated situations, the combination of a limited number (2–4) of reception depths, chosen with physical insight, can increase output SNR, enhance resolution and eliminate possible ambiguities.

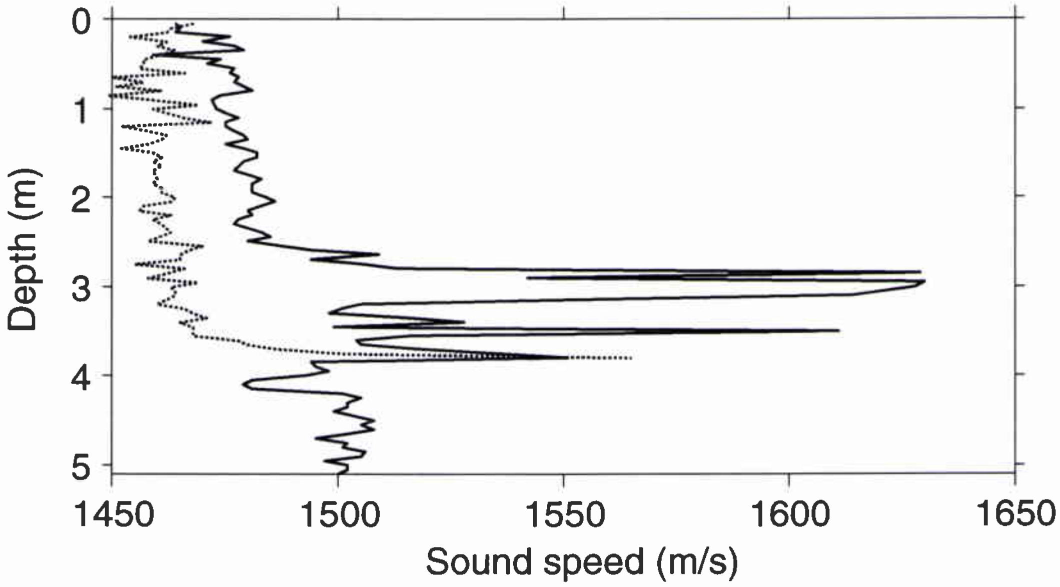

Figure 19 *Range dependence of sound speed and gradient of the top clay layer along the transect XF: core 120 near 7.5 km range (dash) and core 123 near 15 km range (solid).*

5.11 RD versus RI Inversion

Higher resolution of the clay SSP (top speed c_{clay} and gradient ∂c_{clay}) was achieved with RD inversion. For these runs, the search ranges were extended and the other bottom parameters were held fixed (Table 2). The range dependence of ocean SSP, water depth and top layer thickness was incorporated into the coupled normal mode modeling. RI inversion runs of c_{clay} and Δz_{clay} which assumed $\partial c_{\text{clay}} = 0$ m/s were performed for comparison. Results are summarized in Table 4 for the four ranges. The median (S row) and semi-interquartile range (Q) of the 32 single-depth bottom inverses are given to describe their central tendency and dispersion.

The space-coherent, depth-average and single-depth (discretized) bottom estimates are close or equal, and in good agreement with the *in situ* geophysical data.

In single-depth RD inversion runs, the sensitivity to ∂c_{clay} was noticeably improved compared to the preceding RI runs [∂c_{clay} statistics in Fig. 17]. It is remarkable that changes in the c_{clay} and ∂c_{clay} RD estimates reflect the range dependence of the clay layer SSP along the transect XF as observed on cores 123 (15 km), 120, 18, and 8 (7.5 km), and 9 (0 km) in Figs. 19 and 24, and Fig. 12 in [13]. The RD9 c_{clay} and ∂c_{clay} values fit well the SSP measured on core 18 (Fig. 24). The previous RI9 estimate $\partial c_{\text{clay}} = 3\ \text{s}^{-1}$ is consistent with the RD4, RD6 and RD9 estimates. The larger differences between the RI15 and RD15 objective values are explained by

Table 4 *RI and RD inversion results at the four ranges*

	RI model				RD model			
	ϕ,ψ	Φ,Ψ (dB)	c_{clay} (m/s)	Δz_{clay} (m)	ϕ,ψ	Φ,Ψ (dB)	c_{clay} (m/s)	∂c_{clay} (s^{-1})
$R = 4.5$ km								
C	0.71	6.9	1480	7.0	0.73	7.0	1475	3.0
A	0.75	2.1	1480	7.0	0.77	2.3	1475	3.0
S			*1485*	*7.2*			*1475*	*2.7*
Q			*7*	*0.9*			*5*	*0.7*
$R = 6$ km								
C	0.80	11.2	1485	8.0	0.80	11.1	1475	2.5
A	0.81	2.6	1485	8.0	0.80	2.5	1475	2.5
S			*1480*	*7.5*			*1475*	*2.5*
Q			*2*	*0.2*			*4*	*1.0*
$R = 9$ km								
C	0.78	10.9	1480	7.0	0.76	10.7	1465	4.5
A	0.82	3.0	1485	8.0	0.79	2.6	1470	3.0
S			*1480*	*7.0*			*1465*	*4.5*
Q			*2*	*0.5*			*7*	*1.2*
$R = 15$ km								
C	0.80	6.2	1490	8.5	0.69	4.9	1465	4.0
A	0.84	4.6	1490	8.5	0.70	2.7	1460	5.0
S			*1490*	*8.5*			*1465*	*4.0*
Q			*1*	*0.1*			*15*	*2.5*

The maxima of MBMF peak level (ϕ,ψ) and gain (Φ,Ψ), and corresponding parameter values are given. Space-coherent (C), depth-average (A) and single-depth (S) discretized results are compared. For single depth, median (S) and semi-interquartile range (Q) values calculated from the 32 depths processed separately are given. Fixed parameter values are: $\rho_{\text{clay}} = 1.5$, $\beta_{\text{clay}} = 0.06$ dB/λ, $\partial c_{\text{clay}} = 0$ s^{-1} (RI model), $\rho_{\text{silt}} = 1.8$, $\beta_{\text{silt}} = 0.15$ dB/λ, and $c_{\text{silt}} = 1530$ m/s.

the local c_{p} increase in the depression bottom (Fig. 5) made of more consolidated sediments. The RD inversion model did not allow c_{silt} to vary with range so that the RI model was more robust at that range.

Compared to RI inversion with gradient search, the forced zero-gradient condition reduced the maxima by only a fraction of a decibel. The RI estimates of c_{clay} and Δz_{clay} represented depth- and range-averages consistent with RD inversion. For example, the RI6 value equals the RD equivalent as calculated from c_{clay} $\partial c_{\mathrm{clay}}$, i.e.

$$1485 \text{ m/s} = (1475 \text{ m/s} + 2.5 \text{ s}^{-1} \times 8 \text{ m})/2. \tag{34}$$

The inverted thicknesses of the top layer are close to the range-averaged stratigraphic data (8.1–6.9 m from Table II in [13]). However the thinning of the top layer 6 km away from the VA was not detected by RI inversions.

The mutual consistency of the inversion results obtained with different model parameterizations and data realizations for different ranges demonstrated the robustness of MBMF inversion. The bottom inverses represent reliable range integrals of the *in situ* direct geophysical/geoacoustic observations. The resolution of RI inversion was limited by ocean and bottom variability, mostly by the range dependence of the thermocline and top layer thicknesses accounted for in the RD inversion.

5.12 *Parametric Optimization*

Having examined the resolution performance of MBMF inversion over a large parameter search space, standard optimization methods were investigated in terms of their accuracy and execution efficiency. A constrained nonlinear optimization algorithm based on state-of-the-art sequential quadratic programming method [48] and line search strategy [49] was implemented [50].

The inverse problem is stated as

$$\mathrm{maximize}_{\mathbf{p}\in\Pi} O(\mathbf{p})P(O), \;\; \Pi = \{\mathbf{p} \in \Re^8\} \tag{35}$$

subject to:

$$\begin{aligned} \mathbf{p}_{\mathrm{l}} \;\le\; \mathbf{p} &\;\le\; \mathbf{p}_{\mathrm{u}} \\ \rho_{\mathrm{clay}} - \rho_{\mathrm{silt}} &\;\le\; 0 \\ \beta_{\mathrm{clay}} - \beta_{\mathrm{silt}} &\;\le\; 0 \\ c_{\mathrm{clay}} + \partial c_{\mathrm{clay}} \Delta z_{\mathrm{clay}} - c_{\mathrm{silt}} &\;\le\; 0 \end{aligned}$$

where $\mathbf{p} = [\rho_{\mathrm{clay}}, \beta_{\mathrm{clay}}, c_{\mathrm{clay}}, \partial c_{\mathrm{clay}}, \Delta z_{\mathrm{clay}}, \rho_{\mathrm{silt}}, \beta_{\mathrm{silt}}, c_{\mathrm{silt}}]$; $\mathbf{p}_{\mathrm{l}}$ and $\mathbf{p}_{\mathrm{u}}$ are given in Table 2. The objective O was taken as either Φ, $\overline{\Phi}$ or Ψ with or without penalty function P for $O \le 1$ as discussed earlier.

Fig. 20 shows the $\Phi_k(\mathbf{p})$ iterates of a RI9 optimization run at 55.2 m water depth. The optimization algorithm located the maximum known from the preceding exhaustive search, and terminated typically after a few hundred iterations. Varying starting guesses and termination criteria led to a large percentage of successful solutions. When compared to genetic algorithms applied to BMFP inversion of corresponding multitone data [13] the number of forward modeling runs is much smaller $[O(10^2)$ *versus* $O(10^4)]$.

In the present case, the good performance of such parametric optimization is mainly attributed to the well-behaved underlying ambiguity function as was visualized from its equipotential surfaces. Fig. 21 displays such a surface for a constant value $\overline{\Phi}(\mathbf{p}) = P_{90}[\overline{\Phi}(\mathbf{p})]$ as a function of the three clay parameters.

5.13 Data versus Model Waveguide Impulse Responses

Fig. 22 compares waveguide impulse responses measured (top) on the VA, and their model (bottom) for best-fitting values of the geoacoustic parameters obtained with RD inversion runs for the four ranges (Table 4). The detailed features of the waveguide impulse responses are well reproduced by the model. From the envelope responses (color-coded), measured and predicted distributions of energy in time and depth are nearly identical. The depth-to-depth agreement between data and model real-valued responses (gray lines) is excellent. There are small differences at 15 km range which were explained earlier but main features are preserved. Nearly as good data-model agreement was obtained with RI inversion.

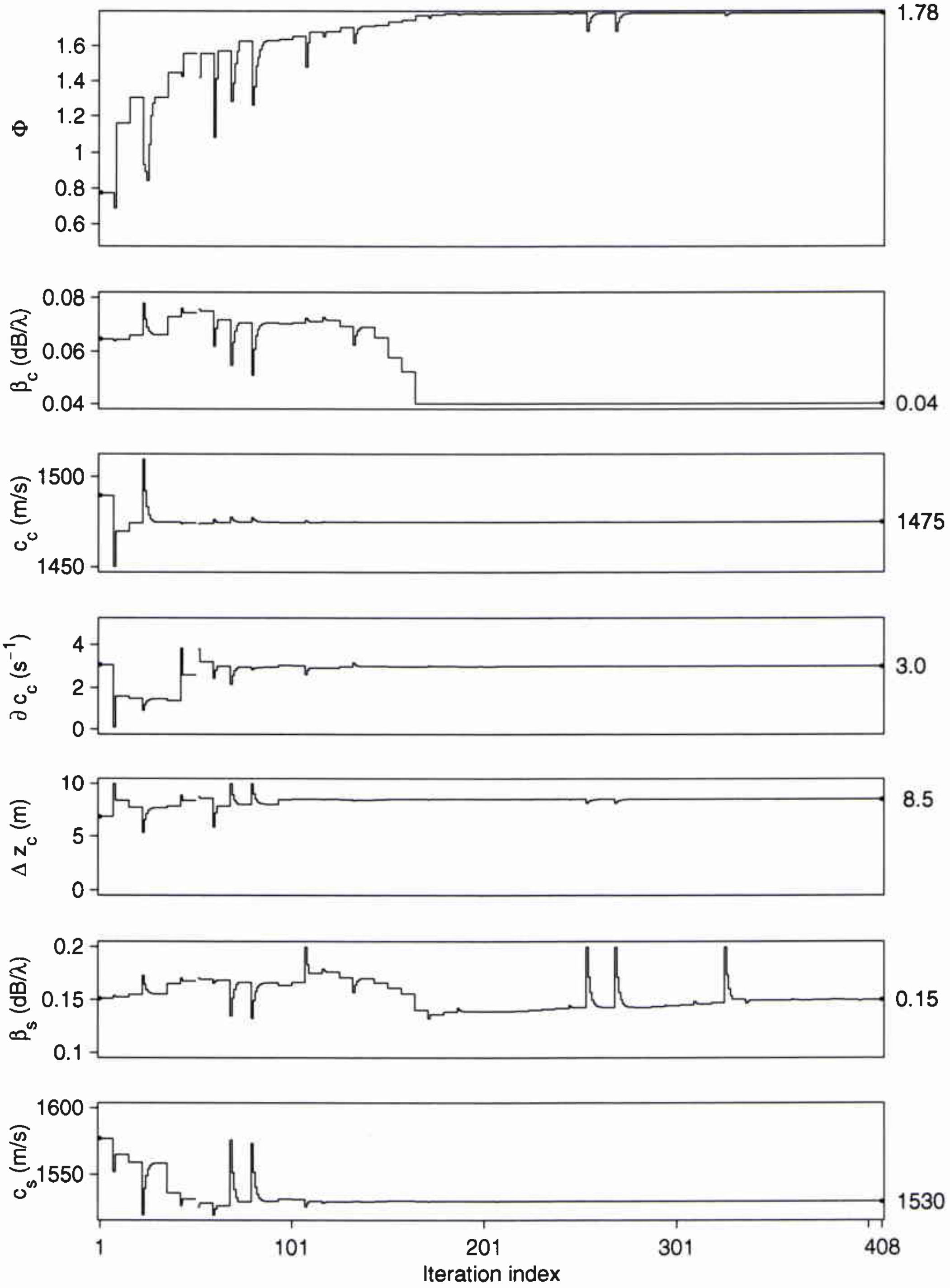

Figure 20 *Objective Φ_k and bottom parameters* $\mathbf{p}$ *convergence for RI9 inversion at 55.2 m depth using a constrained nonlinear optimization algorithm. Subscripts c and s stand respectively for clay and silt.*

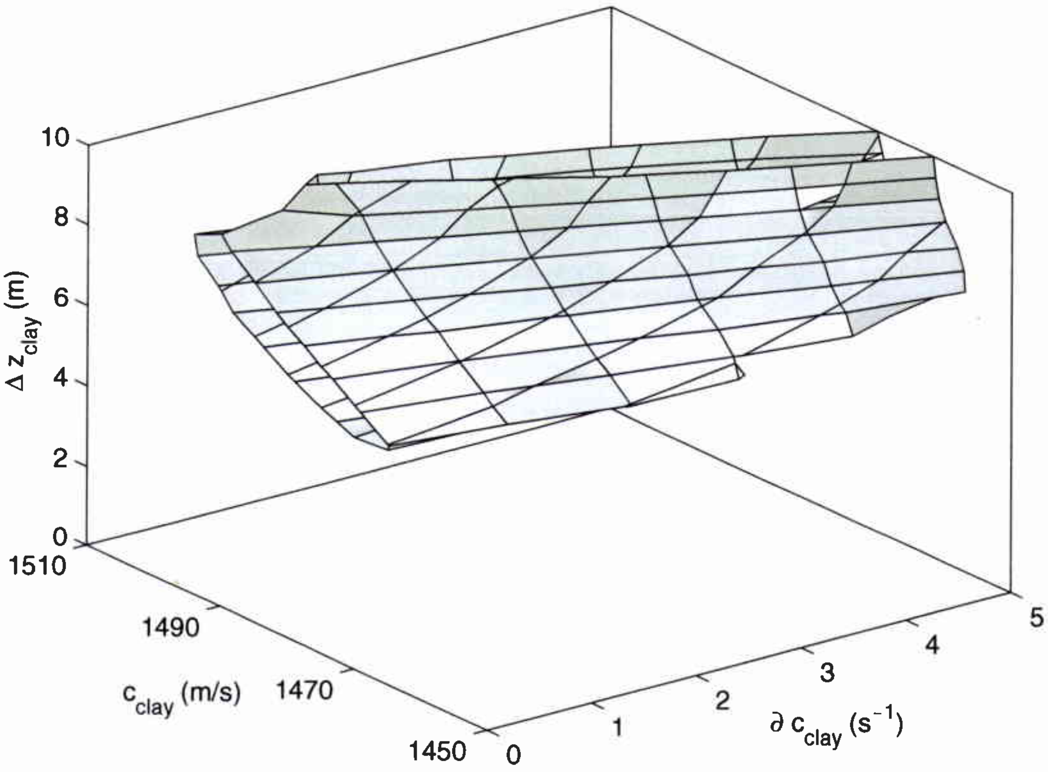

Figure 21 *Objective equisurface* $\overline{\Phi}(c_{\mathrm{clay}}, \partial c_{\mathrm{clay}}, \Delta z_{\mathrm{clay}}) = P_{90}(\overline{\Phi})$ *for* $\beta_{\mathrm{clay}} = 0.04$ dB/λ, $\beta_{\mathrm{silt}} = 0.15$ dB/λ *and* $c_{\mathrm{silt}} = 1530$ *m/s.*

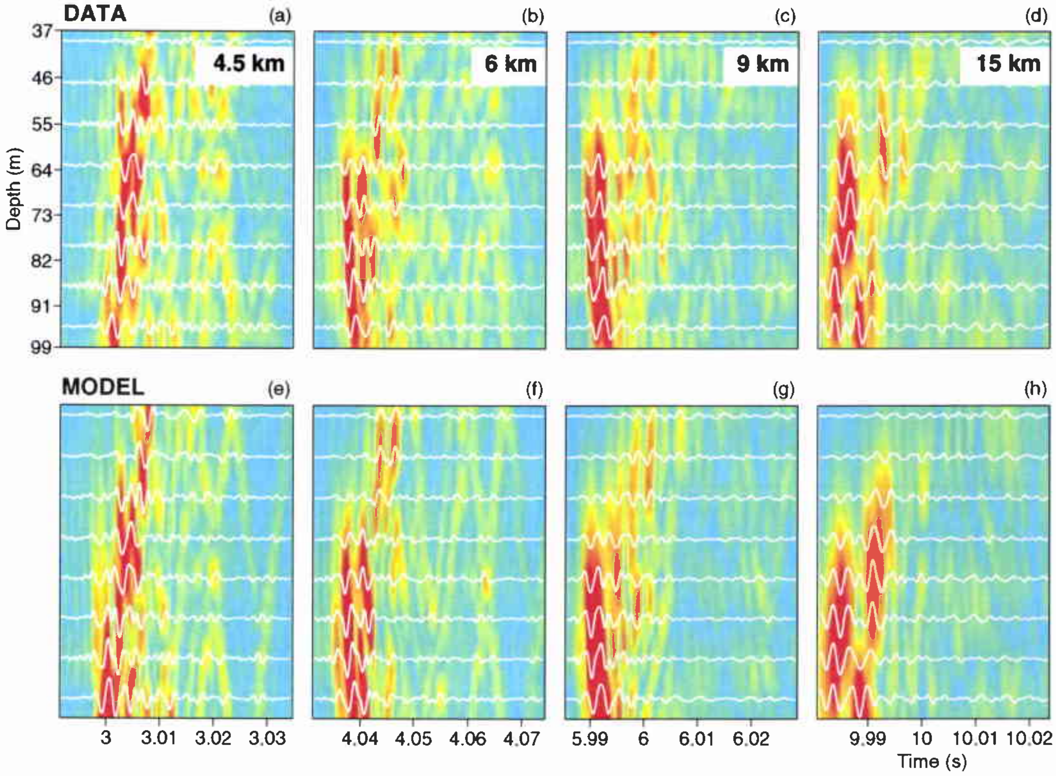

Figure 22 *Measured (top)* versus *modeled (bottom) waveguide impulse responses from RD inversion for the four ranges: (a) 4.5 km, 11 September 1994 1318 UTC ping, (b) 6 km, 11 September 1994 0732 UTC ping, (c) 9 km, 10 September 1994 1808 UTC ping, (d) 15 km, 10 September 1994 1050 UTC ping, (e) RD4, (f) RD6, (g) RD9, and (h) RD15 inversion models. The time scale is the travel time. The water depth scale corresponds exactly to the VA acoustic aperture. Envelope (color-coded) responses are interpolated between the the array elements with normalization to unit total energy. Overlaid real-valued responses (white) are at 39.2 m, 47.2 m, 55.2 m, 63.2 m, 71.2 m, 79.2 m, 87.2 m and 95.2 m depths. The same dynamical range was maintained for the data-model pair of each range.*

6

Discussions and Conclusions

In this paper, we have developed and investigated a single-hydrophone, broad-band, geoacoustic inversion technique. Our main motivation was to demonstrate experimentally that it was possible to invert for bottom properties without resorting to large acoustic receiving apertures, synthetic or real.

The technique is based on broad-band measurements and modeling of the waveguide Green's function. Predicted medium impulse responses for a known geometry and water-column acoustic model unknown (hypothesized) bottom geoacoustic models were incorporated into the reference signal (replica) of a matched filter. The depth-dependent, model-based matched filters (MBMF) were applied to the broad-band signals received on a 63 m 32-element vertical array.

Single-depth and space-coherent objective functions for parametric optimization were derived from the MBMF processing gain relative to the conventional matched filter. This defined a reference level against which candidate bottom models were compared. It corresponds to the free-space Green's function which makes no assumption regarding the propagation medium. Solutions yielding negative gains were definitely rejected while the positive ones were weighted according to their magnitude. This normalization provided more physical insight than a straight correlation coefficient between measurements and predictions.

The band-limited (200–800 Hz) responses were synthesized from CW complex pressure fields calculated by normal-mode models including or not including mode coupling. The inversion models included range-averaged or range-dependent environmental data measured *in situ.*

The inverted parameters were the sound speed profile, attenuation, and thickness of the top layer of soft unconsolidated clay sediments and sound speed and attenuation of the underlying harder silty clay bottom.

Searching the entire parameter space and considering all reception depths were fundamental to performance assessment of MBMF inversion at a single depth.

Range integrals of the bottom properties were determined unambiguously within the constraints imposed by the various parameterizations. The large time-bandwidth product of the propagated signals and the matched filter processing provided considerable robustness against volume and bottom uncertainty and variability without compromizing resolution.

The inversion results were in good agreement with the direct geoacoustic/geophysical measurements from sediment cores and seismic profile. It is emphasized that this type of "ground truthing" should be viewed with caution. Inverse methods are, at least, potentially more accurate and reliable in characterizing the *in situ* geoacoustic properties of the sediment cover than conventional methods. Parameters such as attenuation and sound speed profile are extremely difficult to measure on sediment samples and are subject to spatial aliasing.

Most importantly, the single-depth and space-coherent inversion results obtained for different ranges, depths, signal realizations, and bottom parameterizations were mutually consistent. They also agreed with earlier inversion results from matched-field processing of multitone vertical array data under identical conditions. Comparison of objective statistics showed that the higher resolution and robustness of MBMF inversion was attributable to the *continuum* in place of the discrete frequencies and the intrinsic robustness of the time-domain matched filter.

At a range of 9 km, the space-coherent MBMF gain was 11 dB and single-depth ranged from 2 dB to 5 dB depending on depth. For the clay layer, attenuation, top sound speed, gradient, and thickness were determined as $\beta_{\text{clay}} = 0.05 \pm 0.01$ dB/λ, $c_{\text{clay}} = 1477 \pm 4$ m/s, $\partial c_{\text{clay}} = 2.4 \pm 1.1$ s^{-1} and $\Delta z_{\text{clay}} = 8.7 \pm 0.8$ m, and for the silt bottom, the attenuation and sound speed as $\beta_{\text{silt}} = 0.13 \pm 0.04$ dB/λ and $c_{\text{silt}} = 1532 \pm 5$ m/s. The most sensitive parameters were c_{clay}, Δz_{clay} and c_{silt}.

As range increased, the bottom variability limited the resolution achievable with a range-independent inversion model. Resolution of the bottom sound speed gradient was enhanced by accounting for the range dependence of water-column sound speed profile and depth and upper-sediment-layer thickness measured *in situ*, in the coupled normal mode model. Comparison of results for different ranges showed that the known variations of the bottom sound speed profile were correctly integrated.

Space-coherent processing of all possible VA signal combinations showed that the highest MBMF peak level (13 dB) and resolution were attained with only 2–4 hydrophones optimally distributed in depth, depending on the wavefield complexity. This was explained by redundancy in the spatiotemporal structure and verified by simulations based on the experimental conditions. Likewise the sensitivity of single-depth MBMF processing to varying bottom parameters was, for many depths, higher than space-coherent over the entire array.

Finally, it was shown that the well-behaved ambiguity functions permitted the use of constrained nonlinear optimization methods in place of combinatorial searches, thereby considerably reducing the execution time.

In conclusion, even for the fairly complex environmental conditions of *Yellow Shark* a *single* transmission of a broad-band-coded signal received at a *single* depth, and a few hundred forward modeling runs, were sufficient to correctly resolve the bottom features.

The next phase of this research is extending MBMF inversion to a field of advanced drifting acoustic buoys for the rapid assessment of range-dependent bottom properties. Preliminary inversion results of carbonate sands on the western Sicilian shelf agree with expectations from geophysical ground truth [24], demonstrating the general applicability of the single-hydrophone geoacoustic inversion method presented in this paper.

Annex A

Sediment Core Analysis

Core data: In addition to 16 short (0.4–2.1 m) sediment cores obtained in the *Yellow Shark* experimental area (Fig. 2 in [13]) a 5.35 m long core 18 (Figs. 23 and 24) was collected by R/V *Urania* during the *Maremma* sea trials in November 1996. The core was taken with a piston corer at a point close to transect XF where the upper clay layer was sufficiently thin (4 m) to reach the underlying sand and silt layers. Two short (1.3 m) cores 19 and 20 (Fig. 25) of undisturbed surficial sediments were taken with a sediment-water corer by R/V *Alliance* in April 1997 at the same location. These new cores analyzed by CNR Istituto di Geologia Marina of Bologna and SACLANTCEN refined the geo-acoustic model of the Giglio basin platform.

Calibration: Cores 19 and 20, and short (1.4 m) cores 8 and 9 analyzed previously (Fig. 12 in [13], were used to calibrate the compressional wave (sound) speed (c_{p}) profile measured on core 18. The profile had to be corrected for a bias introduced in the measurement of very small travel times (≈ 0.1 ms) over the small diameter (63 mm) and compaction of the soft sediment caused by the liner penetration.

Correlation based on magnetic susceptibility (K) and c_{p} curves showed that core 18 did not recover the uppermost interval of unit 1, i.e. the first 30 cm below the sea floor. This was identified from the apparent trend reversals of K and c_{p} observed in core 18 with respect to cores 19 and 20 (Fig. 26).

The surficial, very soft sediments were probably dispersed away by the compressional wave generated by the piston corer. Taking into account the lost of the uppermost 30 cm of the sedimentary column, a more accurate evaluation of the compaction of core 18 can be attempted. Considering a depth-average c_{p} of 1485 m/s, the real thickness of the sediment layer between the sea floor and the grainstone layer, which is thought to generate the strong reflector at 5.35 ms depth in a corresponding seismic profile, is 397 cm. Thus, subtracting the top 30 cm lost, the stratigraphic thickness represented in the upper half of core 18 should be 367 cm; real thickness measured in core is 270 cm. This results in a mean value of 26% for the compaction in the upper soft sediment unit, with peak values of 50% at the top of the core (see correlation between the cores 18, and 19 and 20 in Fig. 26).

Core description: Core 18 can be divided into three main sedimentary units characterized by distinctive lithology, grain size and physical parameters (Fig. 24). These

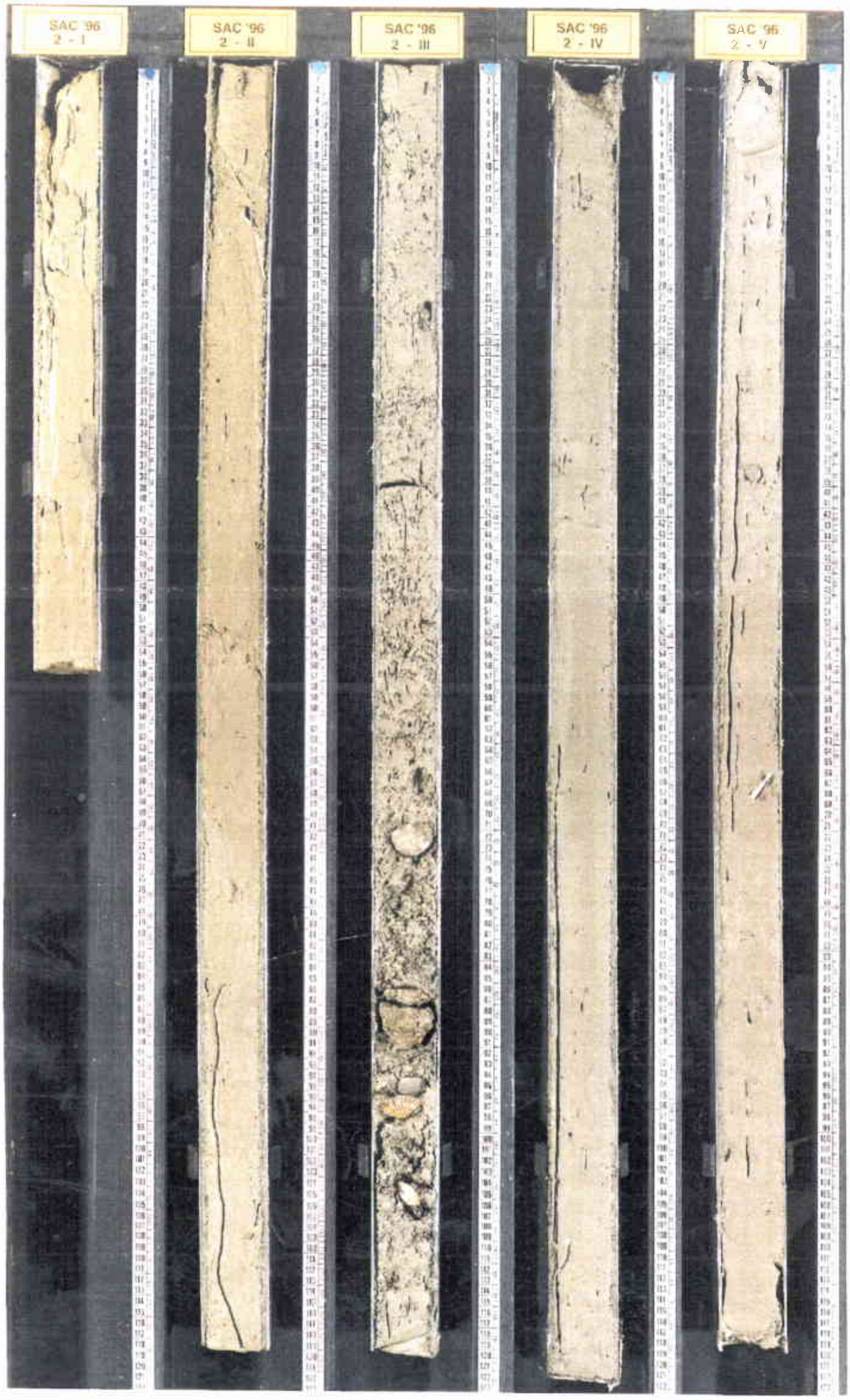

Figure 23 *Photograph of sediment core 18 collected with a piston corer. The coring location is indicated in Fig. 1*

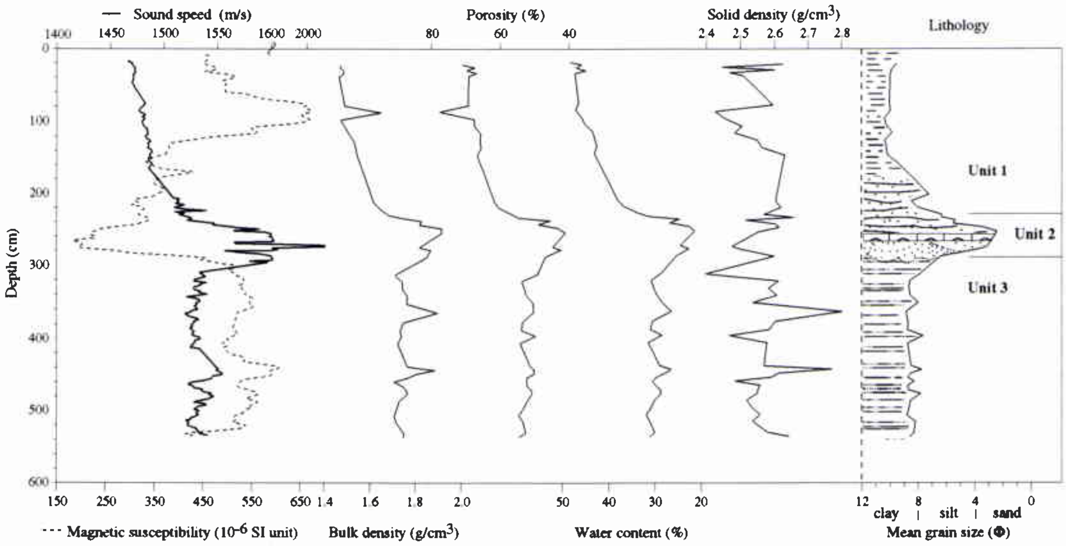

Figure 24 *Compressional wave (sound) speed, magnetic susceptibility, mass properties and lithology* versus *core depth of core 18.*

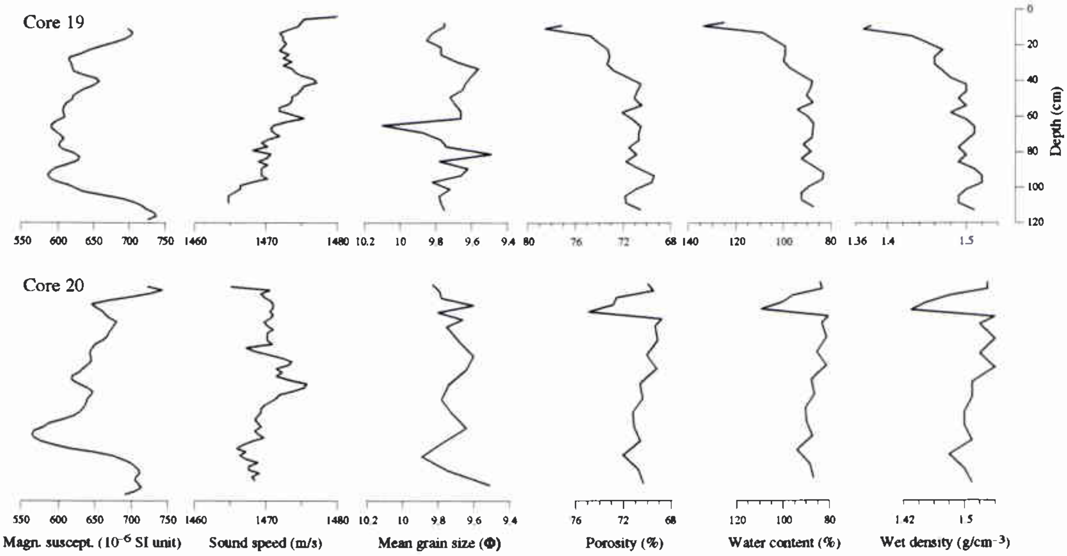

Figure 25 *Sound speed, magnetic susceptibility and mass properties* versus *core depth of cores 19 and 20. Coring locations are indicated in Fig. 1.*

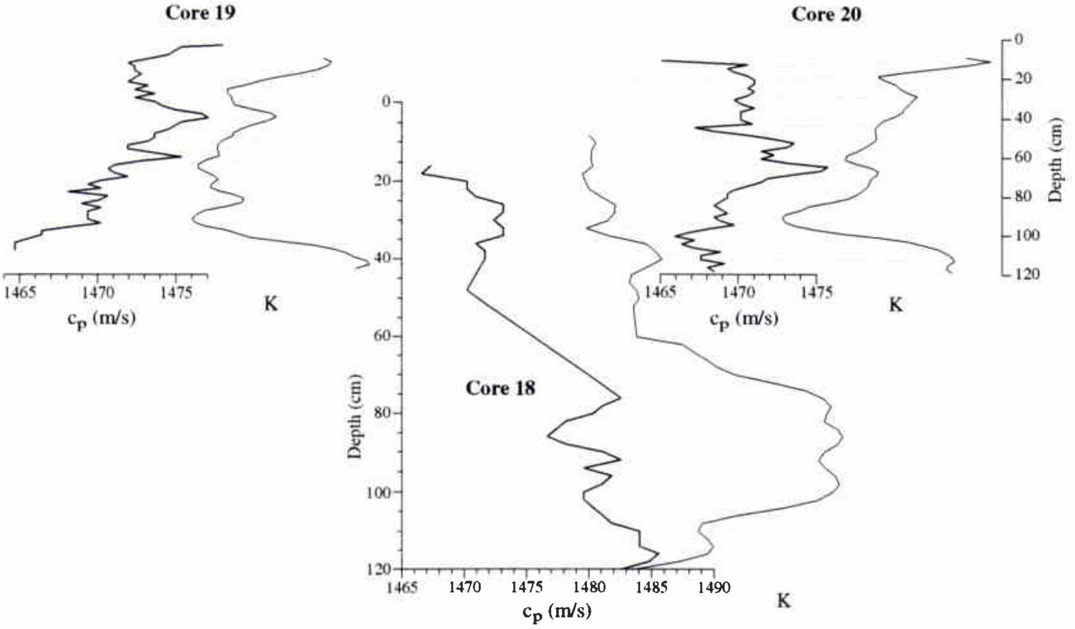

Figure 26 *Calibration of core 18 with sediment-water cores 19 and 20 based on magnetic susceptibility (K) profile.*

units are from the bottom: 3) lower bioturbated mud (285–535 cm); 2) bioclastic muddy sand and biocalcarenite (200–285 cm); 1) upper bioturbated mud (0–200 cm).

Unit 3 is made up of massive grey silty clays with occasional, very thin sand lamina; primary sedimentary structures are not recognizable due to a high degree of bioturbation; the macrofauna is represented by scattered specimens of the mollusks *Turritella sp.* and *Nucula sp.* The top of unit 3 is characterized by an irregular contact with the overlying bioclast-rich unit 2; this contact is partially masked by large burrows cutting the unit 3 and filled with coarser sediment of unit 2. Sound speeds in unit 3 are in good agreement with the other physical parameters; the average value is 1530 m/s with a slight upward increase and scattered peaks in the lower half of the unit. These features match with the observed upward increase of the mean grain size and bulk density and the concomitant decrease of porosity and water content; scattered peaks are related to very thin sand layers, also well detected by magnetic susceptibility, bulk and solid density.

Unit 2 is a sharp-based composite unit made up of three distinct horizons. The lower horizon (275–285 cm) is a structureless, bioclast rich muddy sand; bioclasts are shallow marine mollusk fragments (*Glycimeris sp.*, *Chlamys sp.*). The intermediate horizon (270–275 cm) is a thin, well cemented biocalcarenite layer; thin sections show that this layer can be better defined as a grainstone [51] due to the carbonate nature of its skeletal components (mollusk shells and foraminifera tests), the absence of matrix and the carbonate cement. The upper horizon (200–270 cm) is similar to the lower one in terms of facies characteristics differing only in its higher mud content and well-defined fining-upward trend. Sound speeds reflect well the lithology and physical parameters of the unit; the sharp base is recorded by a sudden speed increase to an average value of 1590 m/s (lower horizon), which corresponds to the abrupt appearance of a fine sand fraction and the consequent increase of bulk density and decrease of porosity values; the mainly carbonatic nature of sand-size clasts is detected well by the abrupt decrease of magnetic susceptibility values. Peak values of sound speed (2200 m/s) and lowest values of magnetic susceptibility correspond to the grainstone layer of the intermediate horizon. The upper horizon exhibits a gradual mean grain size and bulk density upward decrease and a concomitant porosity and water content increase; these trends are perfectly mirrored by the sound speed profile that shows a gradual decrease to an average value of 1570 m/s and by the magnetic susceptibility profile that, on the contrary, shows a gradual upward increase due to the progressive disappearance of the carbonate fraction.

Unit 1 (0–200 cm) is very soft massive yellow-gray clays. Mean grain size curve shows an overall fining-upward trend except for the topmost horizon which is characterized by a reverse coarsening-upward trend, clearly recognizable in cores 19 and 20. The other physical parameters are strictly related to mean grain size variations: bulk density decreases while porosity and water content increase; these trends clearly reflect the degree of compaction of the sediments; Sound speeds in this upper unit are also in excellent agreement with the other physical parameters with a progressive decrease towards the top of the core where values as low as 1460 m/s are measured. The magnetic susceptibility curve shows a complex pattern that apparently does not match with the other parameters; the most prominent feature is a large peak in the intermediate part of the unit, that appears to be related only to a decrease in solid density values; this fact indicates the presence of light ultrafine particles (probably charcoal). Similar magnetic susceptibility peaks have been observed in other cores of the same geographic area at the same stratigraphic level; its detailed characterization and interpretation will be the subject of a future paper.

General stratigraphic framework: The lithologic units recognized in core 18 are well constrained in terms of sedimentary facies and physical parameters; moreover, the vertical stack of these units has a clear stratigraphic meaning; thus, using a sequence stratigraphic approach, core 18 can be read in terms of sedimentary evolution of the depositional site in relation to relative sea-level changes during the last glacial cycle. The outer shelf area of the northern Tyrrhenian sea where core 18 was collected is characterized by a thick succession of pliocene to quaternary marine deposits. High-resolution seismic profiles [52] show that younger deposits are arranged in a vertical stack of thin tabular seismo-stratigraphic units separated by erosional surfaces; the erosional character of such surfaces becomes more evident at shallower depths where small sand bodies with progradational geometries develop above the surfaces around erosional remnants. Core 18 has recovered the youngest seismo-stratigraphic unit (units 1 and 2) and the upper part of the underlying one (unit 3); the irregular contact between units 3 and 2 corresponds to the erosional surface shown by seismic profiles; the strong reflection that is normally associated to such a surface is easily explained by the higher velocity and bulk density values of unit 2 deposits, with respect to the overlying and underlying units. From a stratigraphic point of view, core 18 records the sedimentary history of the northern Tyrrhenian sea outer shelf during the last glacial cycle; shallow marine silty clays of unit 3 were deposited during the sea-level falling stage of the cycle; during the last glacial maximum (ca. 20 kyrs B.P.) the sea level reached its minimum level at -120 m below the present one; in this period shelf areas experienced subaerial condition and an erosional surface developed; during the transgressive stage related to the subsequent rapid sea-level rise, the former subaerial erosional surface was reworked by marine erosional processes; the bioclastic muddy sands at the base of unit 2 were deposited during this phase which is characterized by a dramatic decrease of terrigenous sediment input due to the rapid landward retreat of the shoreline and associated depositional systems with the consequent trapping of sediment in continental settings; sedimentation in shelf areas was characterized by the progressive increase of the biogenic component; during the late phase of the transgression and the early phase of the subsequent high-stand stage, outer shelf areas were almost starved and pure carbonate deposition took place; the relatively long period of starving and the exposition to high-energy marine processes, promoted the early cementation of carbonate deposits; the grainstone layer of unit 2 formed in this phase. The upper part of units 2 and unit 1 were deposited during the high-stand stage of the cycle; in this stage terrigenous input progressively increased due to the slow progradation of coastal depositional systems; carbonate deposition was gradually replaced by terrigenous sediments and outer shelf areas became a quiet muddy environment.

Methodologies: Grain size analyses were performed using standard techniques; fractions coarser than 63 mm were separated with sieves; finer fractions were determined with a Merimitics Sedigraph 5000; porosity, density and water content were obtained by using Beckman 930 gas pycnometer. Sound speed measurements were described in [13].

Whole core magnetic susceptibility was measured at 2 cm intervals with a Bartington MS2 susceptibility meter coupled with a core scanning sensor type MS2C with 100 mm internal diameter. The meaning of magnetic susceptibility is the ease with which a material can be magnetized. Low-field volume magnetic susceptibility (K) is defined as the ratio of induced magnetization intensity (M) per unit volume to the strenght of the applied magnetic field (H) inducing the magnetization ($K = M/H$). In low (< 1 mT) magnetic fields the magnetic moment induced in the material reverts to zero on removal of the applied field [53]. Magnetic susceptibility is *not* a measure of a permanent magnetization and (hence) is *not* related to the earth's magnetic field. Since M and H are measured in units of magnetic field, K is a dimensionless ratio. Magnetic susceptibility is largely a function of mineralogy, but the size and shape of magnetic grains are also of significance. Ferri- and ferromagnetic grains may be divided into three categories: multidomain (MD), single domain (SD) and superparamagnetic (SP) on the basis of the size. Magnetic susceptibility is sensitive to changes in the grain-size across the SP–SD–MD ranges with increasing values occurring for SP and MD domain states. In deep sea sediments this parameter is function of the concentration and composition (mineralogy and grain size) of magnetizable material contained within the core. This material is represented by ferromagnetic minerals (ferrimagnetic and canted antiferromagnetic) as well as paramagnetic minerals (clay and ferromagnesian silicate minerals, iron and manganese carbonates, and some iron sulfides). Magnetic minerals in marine systems can be derived from a variety of sources and several mechanisms may affect their concentration: a) change in supply rate of magnetic minerals from primary sources (terrigenous, volcanogenic, biogenic, hydrothermal, etc.); b) change in accumulation rate of the weakly magnetic component of the sediment; c) authigenic growth of magnetic minerals and/or diagenetic.

Acknowledgement

I wish to acknowledge with gratitude the very real contribution of Dr. E. Michelozzi, SACLANTCEN, and Dr. M. Roveri, C.N.R. Bologna, to this work in analyzing sediment cores and reporting in Appendix A. Special thanks to Dr. F. Chiocci and the crew of R/V *Urania* who collected the deep core during the Maremma sea trials in November 1996. The many people within and outside SACLANTCEN, and the crews of the R/V *Alliance* and *Manning* who participated in the Yellow Shark 94 and 95 sea trials are warmly acknowledged for their outstanding contributions.

References

[1] M. Hinich, "Maximum likelihood signal processing for a vertical array," *Journal of the Acoustical Society of America,* vol. 54, no. 2, pp. 499–503, 1973.

[2] H. P. Bucker, "Use of calculated sound fields and matched-field detection to locate sound in shallow water," *Journal of the Acoustical Society of America,* vol. 59, no. 2, pp. 368–373, 1976.

[3] A. B. Baggeroer, W. A. Kuperman and P. Mikhalevsky, "An overview of matched field methods in ocean acoustics," *IEEE Journal of Oceanic Engineering,* vol. 18, no. 4, pp. 401–424, 1993.

[4] H. P. Bucker, "Matched field tracking in shallow water," *Journal of the Acoustical Society of America,* vol. 96, no. 6, pp. 3809–3811.

[5] J. V. Candy and E. J. Sullivan, "Passive localization in ocean acoustics: A model based approach," *Journal of the Acoustical Society of America,* vol. 98, no. 3, pp. 1455–1471, 1995.

[6] Z.-H. Michalopoulou and M. B Porter, "Matched-field processing for broadband source localization," *IEEE Journal of Oceanic Engineering,* vol. 21, no. 4, pp. 384–391, 1996.

[7] M. D. Collins, W. A. Kuperman, and H. Schmidt, "Nonlinear inversion for ocean bottom properties," *Journal of the Acoustical Society of America,* vol. 92, no. 5, pp. 2770–2783, 1992.

[8] C. E. Lindsay and N. R. Chapman, "Matched field inversion for geophysical parameters using adaptive simulated annealing," *IEEE Journal of Oceanic Engineering,* vol. 18, no. 3, pp. 224–231, 1993.

[9] P. Gerstoft, "Inversion of seismoacoustic data using genetic algorithms and *a posteriori* probability distributions," *Journal of the Acoustical Society of America,* vol. 95, no. 2, pp. 770–782, 1994.

[10] A. Caiti, S. M. Jesus and A. Kristensen, "Geo-acoustic seafloor exploration with a towed array in a shallow water area of the Strait of Sicily," *IEEE Journal of Oceanic Engineering,* vol. 21, no. 4, pp. 347–354, 1996.

[11] G. V. Frisk and J. F. Lynch, "Shallow water waveguide characterization using the Hankel transform,", *Journal of the Acoustical Society of America,* vol. 76, no. 1, pp. 205–216, 1984.

[12] S. D. Rajan, J. F. Lynch and G. V. Frisk, "Perturbative inversion methods for obtaining bottom geo-acoustic parameters in shallow water," *Journal of the Acoustical Society of America*, vol. 82, no. 3, pp. 998–1017, 1987.

[13] J.-P. Hermand and P. Gerstoft, "Inversion of broad-band multitone acoustic data from the Yellow Shark summer experiments," *IEEE Journal of Oceanic Engineering*, vol. 21, no. 4, pp. 324–346, 1996.

[14] *Full Field Inversion Methods in Ocean and Seismo-Acoustics*, O. Diachok, A. Caiti, P. Gerstoft and H. Schmidt, Eds. Dordrecht: Kluwer, 1995.

[15] *Inversion Techniques and the Variability of Sound Propagation in Shallow Water*, Special Issue of the *IEEE Journal of Oceanic Engineering*, vol. 21, no. 4, October 1996.

[16] L. A. Rubano, "Acoustic propagation in shallow water over a low-velocity bottom," *Journal of the Acoustical Society of America*, vol. 67, no. 5, pp. 1608–1613, 1980.

[17] J. Zhou, X. Zhang, P. H. Rogers and J. Jarzynski, "Geoacoustic parameters in a stratified sea bottom from shallow water acoustic propagation," *Journal of the Acoustical Society of America*, vol. 82, no. 6, pp. 2068–2074, 1987.

[18] W. H. Carey, J. Doutt, R. Evans and L. Dillman, "Shallow water sound transmission measurements taken on the New Jersey Continental Shelf," *IEEE Journal of Oceanic Engineering*, vol. 20, no. 4, pp. 321–336, 1995.

[19] N. R. Chapman and C. E. Lindsay, "Matched-field inversion for geo-acoustic model parameters in shallow water," *IEEE Journal of Oceanic Engineering*, vol. 21, no. 4, pp. 347–354, 1996.

[20] G. V. Frisk, J. F. Lynch and S. D. Rajan, "Determination of compressional wave speed profiles using modal inverse techniques in a range-dependent environment in Nantucket Sound," *Journal of the Acoustical Society of America*, vol. 86, no. 5, pp. 1928–1939, 1989.

[21] J. F. Lynch, S. D. Rajan and G. V. Frisk, "A comparison of broad-band and narrowband modal inversions for bottom geo-acoustic properties at a site near Corpus Christi, Texas," *Journal of the Acoustical Society of America*, vol. 89, no. 2, pp. 648–665, 1991.

[22] J.-P. Hermand, F. Spina, P. Nardini and E. Baglioni, "*Yellow Shark* broadband inversion experiment: Environmental data 1994–1995," SACLANT Undersea Research Centre, La Spezia, Italy, 1995, SACLANTCEN CD-ROM *Yellow Shark* series YS-2.

[23] J.-P. Hermand, E. Michelozzi, P. Boni, F. Spina and P. Nardini, "*EnVerse 97* advanced drifting buoy field experiment: Oceanographic and geophysical data,"

SACLANT Undersea Research Centre, La Spezia, Italy, 1998, SACLANTCEN CD-ROM *EnVerse* series EV-1.

[24] J.-P. Hermand, E. Michelozzi, P. Guerrini and A. Barbagelata, "Advanced Drifting Acoustic Buoy Field for Rapid Assessment of Bottom Properties in Shallow Water: EnVerse 97 Experiments," in *Proceedings of the Fourth European Conference on Underwater Acoustics,* A. Allipi and G. B. Cannelli, Eds. Roma: European Commission, 1998, pp. 319–326.

[25] J.-P. Hermand, "Model-based matched filter processing: A broad-band approach to shallow-water inversion," in *Full Field Inversion Methods in Ocean and Seismo-Acoustics,* O. Diachok, A. Caiti, P. Gerstoft and H. Schmidt, Eds. Dordrecht: Kluwer, 1995, pp. 189–194.

[26] J-P. Hermand and W.I. Roderick, "Model-based processing of large time-bandwidth product signals in a time dispersive ducted sound channel," in *Proceedings of the NATO Advanced Study Institute on Acoustic Signal Processing for Ocean Exploration,* J.M.F. Moura and I.M.G. Lourtie, Eds. Dordrecht: Kluwer, pp. 131–138, 1992.

[27] ——, "Acoustic model-based matched filter processing for fading time-dispersive ocean channels: Theory and experiment," *IEEE Journal of Oceanic Engineering,* vol. 18, no. 4, pp. 447–465, 1993.

[28] A. Parvulescu, "Signal detection in a multipath medium by M.E.S.S. processing," *Journal of the Acoustical Society of America,* vol. 33, p. 1674, 1961.

[29] C. S. Clay, "Optimum time domain signal transmission and source localization in a waveguide," *Journal of the Acoustical Society of America,* vol. 81, no. 3, pp. 660–664, 1987.

[30] J.-P. Hermand and R. Soukup, "Broadband inversion experiment *Yellow Shark* '95: Modelling the transfer function of a shallow-water environment with a range-dependent soft clay bottom," in *Proceedings of the Third European Conference on Underwater Acoustics,* J. S. Papadakis, Ed., Heraklion, Crete, 1996, pp. 931–936.

[31] M. Siderius and J.-P. Hermand, "Yellow Shark Spring 95: Inversion results from sparse broad-band acoustic measurements over a highly range dependent soft clay layer," submitted to *Journal of the Acoustical Society of America,* 1998.

[32] T. Akal, C. Gehin, B. Matteucci, and B. Tonarelli, "Measured and computed physical properties of sediment cores, Island of Elba zone," SACLANT Undersea Research Centre, La Spezia, Italy, 1972, SACLANTCEN document M-82.

[33] S. W. Golomb, *Shift Register Sequences,* rev. ed. Laguna Hills, CA:Aegean Park Press, 1982.

[34] L. Cohen and C. Lee, "Instantaneous bandwidth for signals and spectrograms," *Proc. IEEE ICASSP-90*, pp. 2451–2454, 1990.

[35] E. Michelozzi, P. Guerrini, R. Chiarabini, B. Tonarelli and M. C. Mori, "*Yellow Shark* core data analysis," SACLANT Undersea Research Centre, La Spezia, Italy, 1996, SACLANTCEN unpublished document.

[36] E. Michelozzi, "Quaternary sediments in the Elba-Formiche islands basin," SACLANT Undersea Research Centre, La Spezia, Italy, 1994, SACLANTCEN document IN-678.

[37] F. C. Wezel, D. Savelli, M. Bellagamba, M. Tramontana, and R. Bartole, "Plio-quaternary depositional style of sedimentary basins along insular tyrrhenian margins: Sedimentary basins of mediterranean margins," F. C. Wezel Ed. Bologna, pp. 239–270, 1981.

[38] F. L. Chiocci, L. Orlando and P. Tortora, "Small-scale seismic stratigraphy and paleogeographical evolution of the continental shelf facing the SE Elba Island (Northern Tyrrhenian Sea, Italy)," *Journal of Sedimentary Petrology,* vol. 61, no. 4, pp. 506–526, 1991.

[39] F. B. Jensen, "Comparison of transmission loss data for different shallow-water areas with theoretical results provided by a three-fluid normal-mode propagation model," in O. F. Hastrup and O. V. Oleson Eds., *Sound Propagation in Shallow Water, Vol. II*, SACLANT Undersea Research Centre, La Spezia, Italy, 1974, SACLANTCEN document CP-14, pp. 79–92.

[40] S. Kirkpatrick, C. D. Gelatt and M. P. Vecchi, "Optimization by simulated annealing," *Science*, 220, pp. 671–680, 1983.

[41] D. E. Goldberg, *Genetic Algorithm in Search, Optimization and Machine Learning,* New York, NY: Addison Wesley, 1988.

[42] J.-P. Hermand, W. Roderick, P. Guerrini, L. Gualdesi and F. De Strobel, "Phase Speed and Pressure Field Measurements with a Towed Oceanographic and Acoustic Profiler: Yellow Shark 95 Geo-Acoustic Inversion Results," in *Proceedings of the Fourth European Conference on Underwater Acoustics,* A. Allipi and G. B. Cannelli, Eds. Roma: European Commission, 1998, pp. 339–346.

[43] F. B. Jensen, W. A. Kuperman, M. B. Porter and H. Schmidt, *Computational Ocean Acoustics,* R. T. Beyer Ed. New York: AIP Press, 1994.

[44] F. B. Jensen and M. C. Ferla, "SNAP—The SACLANTCEN normal mode acoustic propagation model," SACLANT Undersea Research Centre, La Spezia, Italy, 1979, SACLANTCEN document SM-121.

[45] M. C. Ferla, M. B. Porter and F. B. Jensen, "C-SNAP: coupled SACLANTCEN normal mode propagation loss model," SACLANT Undersea Research Centre, La Spezia, Italy, 1993, SACLANTCEN document SM-274.

[46] O. F. Hastrup, "Some bottom-reflection loss anomalies near grazing and their effect on propagation in shallow water," in *Bottom-Interacting Ocean Acoustics,* W. Kuperman and F. Jensen Eds. New York: Plenum, 1980, pp. 135–152.

[47] J. W. Tukey, *Exploratory Data Analysis,* Addison-Wesley Publishing Company, 1977.

[48] P. E. Gill, W. Murray, and M. H. Wright, *Practical Optimization,* London, Academic Press, 1981.

[49] M. J. D. Powell, "A fast algorithm for nonlinearly constrained optimization calculations," in *Numerical Analysis,* G. A. Watson, Ed., Lecture Notes in Mathematics, vol. 630, Springer Verlag, 1978.

[50] *NAG Fortran Library Manual Mark 15,* vol. 4, E04, 1991.

[51] R. J. Dunham, "Classification of carbonate rocks according to depositional texture," *Mem. Am. Assoc. Pet. Geol .,* vol. 1, pp. 108–121, 1962.

[52] E. Aiello, C. Bartolini, E. Brizzolari, C. Clerici, L. Orlando, and L. Salvati, "Studio della piattaforma continentale medio-tirrenica per la ricerca di sabbie metallifere: 3) dal Canale di Piombino al Golfo Stella (Isola d' Elba)," *Boll. Soc. Geol. It.,* vol. 99, pp. 319–340, 1980.

[53] D. W. Collinson, *Methods in Rock Magnetism and Paleomagnetism—Techniques and instrumentation,* New York:Chapman and Hall, pp. 1–503, 1983.

Report no. changed (Mar 2006): SM-359-UU

Document Data Sheet

Security Classification UNCLASSIFIED		*Project No.* 013-1
Document Serial No. SM-359	*Date of Issue* May 1999	*Total Pages* 69 pp.

Author(s)

Hermand, J.-P.

Title

Broad-band geoacoustic inversion in shallow water from waveguide impulse response measurements on a single hydrophone: theory and experimental results.

Abstract

Performance models such as the Allied Environmental Support System (AESS) require environmental input parameters such as the geoacoustic properties of the battlespace. The models ingest the input parameters from databases to predict the ASW and MCM performance in the operating area. These databases have a scarcity of data, particularly in littoral environments. A Rapid Environmental Assessment (REA) technique has been developed which allows for the determination of the geoacoustic properties without resorting to large acoustic receiving apertures. The method is based on reception of broadband acoustic signals and modelling the littoral environment between the acoustic transmitter and a signal receiving hydrophone. In addition, the technique has been extended to drifting sonobuoys such that the bottom properties of the battlespace can be determined remotely. This report presents the measurement and modelling results and demonstrates that the bottom features can be resolved.

Keywords

Issuing Organization

North Atlantic Treaty Organization
SACLANT Undersea Research Centre
Viale San Bartolomeo 400, 19138 La Spezia, Italy

[From N. America: SACLANTCEN
(New York) APO AE 09613]

Tel: +39 0187 527 361
Fax:+39 0187 524 600

E-mail: library@saclantc.nato.int

Report no. changed (Mar 2006): SM-359-UU

Initial Distribution for Unclassified SM-359

Scientific Committee of National Representatives

SCNR Belgium	1
SCNR Canada	1
SCNR Denmark	1
SCNR Germany	1
SCNR Greece	1
SCNR Italy	1
SCNR Netherlands	1
SCNR Norway	1
SCNR Portugal	1
SCNR Spain	1
SCNR Turkey	1
SCNR UK	1
SCNR USA	2
French Delegate	1
SECGEN Rep. SCNR	1
NAMILCOM Rep. SCNR	1

National Liaison Officers

NLO Canada	1
NLO Denmark	1
NLO Germany	1
NLO Italy	1
NLO Netherlands	1
NLO Spain	1
NLO UK	3
NLO USA	4
Sub-total	30
SACLANTCEN library	21
Total	51